Chronostratigraphy of a 270-ka sediment record from Lake Selina, Tasmania: Combining radiometric, geomagnetic and climatic dating

Agathe Lisé-Pronovost, Michael-Shawn Fletcher, Quentin Simon, Zenobia Jacobs, Patricia Gadd, David Heslop, Andy I.R. Herries, Yusuke Yokoyama, Team Aster

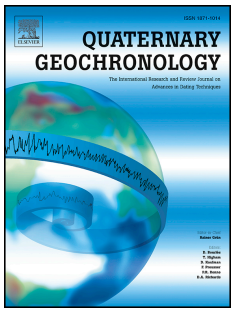

Chronostratigraphy of a 270-ka sediment record from Lake Selina, Tasmania: Combining radiometric, geomagnetic and climatic dating

Agathe Lisé-Pronovost, Michael-Shawn Fletcher, Quentin Simon, Zenobia Jacobs, Patricia S. Gadd, David Heslop, Andy I.R. Herries, Yusuke Yokoyama, Aster team

PII: S1871-1014(21)00003-0

DOI: https://doi.org/10.1016/j.quageo.2021.101152

Reference: QUAGEO 101152

To appear in: *Quaternary Geochronology*

Received Date: 19 February 2020

Revised Date: 11 January 2021

Accepted Date: 12 January 2021

Please cite this article as: Lisé-Pronovost, A., Fletcher, M.-S., Simon, Q., Jacobs, Z., Gadd, P.S., Heslop, D., Herries, A.I.R., Yokoyama, Y., team, A., Chronostratigraphy of a 270-ka sediment record from Lake Selina, Tasmania: Combining radiometric, geomagnetic and climatic dating, *Quaternary Geochronology* (2021), doi: https://doi.org/10.1016/j.quageo.2021.101152.

Chronostratigraphy of a 270-ka sediment record from Lake Selina, Tasmania: combining radiometric, geomagnetic and climatic dating

Agathe Lisé-Pronovost 1,2, Michael-Shawn Fletcher 3, Quentin Simon 4, Zenobia Jacobs 5, Patricia S Gadd 6, David Heslop 7, Andy I.R. Herries 2, Yusuke Yokoyama 8, ASTER team 4,*

1 School of Earth Sciences, University of Melbourne, Carlton, 3053, VIC, Australia

2 The Australian Archaeomagnetism Laboratory, Palaeoscience Labs, Department of Archaeology and History, La Trobe University, Melbourne Campus, Bundoora, 3086, VIC, Australia

3 School of Geography, University of Melbourne, Carlton, 3053, VIC, Australia

4 CEREGE UM34, Aix Marseille Univ, CNRS, IRD, INRAE, Coll France, 13545 Aix en Provence, France

5 Australian Research Council Centre of Excellence for Australian Biodiversity and Heritage and School of Earth, Atmospheric and Life Sciences, University of Wollongong, Wollongong, NSW 2522, Australia

6 Australian Nuclear Science and Technology Organisation (ANSTO), New Illawarra Road, Lucas Heights 2234, Australia

7 Research School of Earth Sciences, Australian National University, Acton 2601, ACT, Australia

8 Department of Earth and Planetary Sciences, Graduate School of Science, University of Tokyo, Chiba 277-8564, Japan

*Georges Aumaître, Didier L. Bourlès, Karim Keddadouche.

Declarations of interests: none.

Keywords

paleomagnetism, optically stimulated luminescence, radiocarbon, authigenic 10Be/9Be ratio, Pleistocene, lake sediment, Australia

Highlights

- Chronostratigraphy of a 266 ± 8 ka continuous lake sediment archive from Australia
- We combine radiometric (^{14}C, OSL) and relative dating (geomagnetic and climatic)
- Bayesian modeling and dynamic programing integrate dating constraints
- First identification of the Laschamp geomagnetic excursion in Australia

Abstract

Lake sediment archives covering several glacial cycles are scarce in the Southern Hemisphere and they are challenging to date. Here we present the chronostratigraphy of the oldest continuous lake sediment archive in Tasmania, Australia; a 5.5 m and 270 ka (Marine Isotope Stage 8) sediment core from Lake Selina. We employ radiometric dating (radiocarbon and optically stimulated luminescence) and relative dating (geomagnetic and climate comparisons). Bayesian modeling of the radiometric ages reaches back to 80 ka (1.7 m) and relative dating using a dynamic programing algorithm allows dating of the full sequence. Elemental data, magnetic properties and beryllium isotopes from Lake Selina reveal a close fit to Antarctic ice core climate proxies. Weaker correlation during the Last Glacial Period (MIS 2–4) is attributed to additional local factors impacting Lake Selina proxies at a time of climate changes and human arrival into Tasmania. Over that period, full vector paleomagnetic records and authigenic $^{10}Be/^{9}Be$ ratios are combined to identify the Laschamp geomagnetic excursion for the first time in Australia and constrain the chronology. The multi-method approach provides two preferred age models, indiscernible within their uncertainties, which allows the use of a geomagnetic dipole-independent (full archive) or a climate-independent (111 ka to present) age model.

1. Introduction

Lake sediments preserve some of the best continuous records of rapid environmental changes, but those covering multiple glacial-interglacial cycles are notoriously difficult to date. At present, only one such long continental record is found on the island of Tasmania, south of mainland Australia (Darwin Crater, Howard and Haines, 2007; Lisé-Pronovost et al., 2019a). Long archives of environmental change from Tasmania have the potential to elucidate how terrestrial environments respond to large-scale and rapid climatic change in an under-documented region of the Southern Hemisphere. Further, developing a precise chronostratigraphy for lake sediments covering the Last Glacial Period in Australia offers the possibility of investigating the timeline and linkages of environmental changes across the local and broader region, shedding light on Earth system dynamics and contributing to debated issues such as megafauna extinction (Roberts et al., 2001; Wroe and Field, 2006; Rule et al., 2012; Van der Kaars et al., 2017; Saltré et al., 2019) and the impact and timing of human arrival on the Australian continent (Cosgrove, 1999; Clarkson et al., 2017; O'Connell et al., 2018). The lacustrine sediments from Lake Selina, a Tasmanian record argued to span the Last Glacial Cycle (Colhoun et al., 1999), provide an opportunity to explore these questions, but their tractability depends on the ability to obtain a reliable chronology.

Dating lacustrine sediments beyond the range of radiocarbon (>40–50 ka) is challenging. An ability to combine different dating methods is therefore key to obtaining a reliable chronology (e.g. Colman et al., 2006; Shanahan et al., 2013; Simon et al., 2020a). Commonly used numerical dating methods for lacustrine sediments include radiocarbon dating of organic material, optically-stimulated luminescence dating of quartz and feldspar, U-series dating of carbonates, varve counting, and ash dating. Other chronological methods include correlation of climate signals (wiggle-matching), tephrochronology, and paleomagnetic dating. An important consideration in the application of multiple methods for developing chronologies is to avoid circular reasoning; i.e., ensuring the use of dating methods that are independent of the variable you are attempting to reconstruct or infer from analysis of the lake sediments (Blaauw et al., 2012). For example, avoid climate comparison if you discuss past climate, and avoid magnetostratigraphy if you discuss the Earth's magnetic field.

Paleomagnetic dating is useful at the multi-millennial timescale using paleosecular variations of the geomagnetic field and major instabilities such as polarity reversals and excursions (Channell et al., 2020). Regional (sub-millennial) paleomagnetic dating is currently infeasible in Australia because there is a critical lack of empirical data required to build paleomagnetic reference curves, a limitation that also biases geomagnetic field models (e.g. Panovska et al., 2015; Constable et al., 2016). The available Pleistocene sedimentary paleomagnetic data from Australia span the past 16 ka and includes only two full vector lacustrine records from northeast Australia (Lake Eacham and Barrine, Constable, 1985; Constable and McElhinny, 1985), four directions-only lacustrine records from southeast Australia (Lake Bullenmerri, Lake Keilambete, Lake Gnotuk, 10 ka, Barton and McElhinny 1981; Lake Johnston, 9.5 ka, Ankers et al., 2001) and two directions-only lagoon records from southeast Australia (Big Jibbon Lagoon 5 ka, and Tocal Homestead Lagoon 2 ka, Gale et al., 2013).

Importantly, none of these previous Australian studies meet the modern standards of laboratory experiments and analytical methods (e.g. Korte et al., 2019), such as magnetic mineral characterisation to identify the magnetic remanence carriers and assess the reliability of the paleomagnetic record. Moreover, while it is now routine to perform stepwise demagnetisation to identify a stable and reliable characteristic remanent magnetisation (ChRM) and calculate the paleomagnetic directions from the best least-squares line fit by principal component analysis (Kirschvink, 1980), available Australian studies employ either single step alternating field (AF) 'blanket' demagnetisation or no demagnetisation at all. New state-of-the-art high-quality sedimentary paleomagnetic and archaeomagnetic data are necessary to confidently isolate the geomagnetic signal from environmental biases and start building Australian regional reference curves (sub-millennial behavior). In the meantime, global geomagnetic dipole moment variation can be used for millennial-timescale paleomagnetic dating by correlating individual records to relative paleointensity (RPI) stacks (e.g. GLOPIS, Laj et al., 2004) or models (e.g. GGF100k, Panovska et al., 2018).

An alternative means for reconstructing millennial-scale geomagnetic dipole moment variations is through reconstructing the concentration of cosmogenic radionuclide beryllium-10 (^{10}Be) deposited in natural archives (Lal and Peters, 1967). Atmospheric ^{10}Be is produced by spallation reactions when highly energetic galactic cosmic ray (GCR) particles interact with nitrogen and oxygen atoms. The incoming rate of these charged GCRs, which directly controls ^{10}Be production rate, depends on the strength of geo- and heliomagnetic fields, with a nonlinear inverse relationship: i.e. lower ^{10}Be production rate at high fields (Beer et al., 2012). In a similar manner to RPI representing paleomagnetic field intensity by removing depositional and environmental influences (King et al., 1983; Roberts et al., 2013), normalised ^{10}Be concentrations from sediment and ice records trace production variations that are mainly modulated by geomagnetic field strength at the millennial timescale (e.g. Frank et al., 1997; Muscheler et al., 2005; Horiuchi et al., 2016; Simon et al., 2016a, 2018). Normalised ^{10}Be can therefore be employed along with RPI proxies to evaluate their respective limitations (Suganuma et al., 2010, 2011; Valet et al., 2014, 2019; Simon et al., 2019, 2020b) and help recovering reliable records of paleomagnetic dipole moment variations from lacustrine sedimentary sequences (Nilsson et al., 2011; Du et al., 2018; Tang et al., 2019).

In this study, we present the chronostratigraphy of Lake Selina in Tasmania, Australia, combining radiocarbon, optically stimulated luminescence (OSL) dating, full-vector sedimentary paleomagnetism, authigenic ^{10}Be /^{9}Be ratio, and climate comparison.

2. Regional setting

Lake Selina (41°52'41"S, 145°36'34"E) is a shallow basin located in the West Coast Range of Tasmania, southeast Australia, 516 meters above sea level (m asl) and 40 km east of the Southern Ocean (Fig. 1). The modern lake has a surface area of 190 m^2 and maximum water depth of approximately 5 m. It has no permanent inflow or outflow; but an ephemeral creek connects Lake Selina to the larger and higher altitude Lake Westwood (380 m^2, 605 m asl) ~1 km to the west. The local geology is dominated by the Ordovician Owen Conglomerate and Cambrian Mount Read Volcanics. The Owen Conglomerate is a coarse siliciclastic molasse with hematite-stained quartz and rounded to sub-rounded quartzite pebbles and cobbles in an argillite matrix (Bradley, 1954). While Mount Selina (~1 km to the east) was prospected for lead and zinc mining, the local mining activities are associated with the Mount Read Volcanics and include the Rosebery mine for galena at ~12 km distance and the Henty gold mine ~5 km distance from Lake Selina (Fig. 1C).

The climate in western Tasmania is temperate maritime with average temperature ranging from 6 to 16°C and average annual rainfall of 2400 mm (Queenstown; Australian Bureau of Meteorology). Pleistocene glacial activity has been documented in Tasmania for the Last Glacial Period (MIS 2–3; Colhoun 1985; Mackintosh et al., 2006) and before, however, with poor age constraints (possibly MIS 4, 6, 8, and/or 10, 12; Barrows et al., 2002; Augustinus et al., 2017). The West Coast Range has many cirques and moraines, which provide evidence of paleo-glaciers at Mount Murchison (1279 m asl) to the north of Lake Selina, Mount Tyndall (1179 m asl) to the south, and Eldon Range (1440 m asl) to the east. Previous coring of the uppermost 4 m sediments at Lake Selina revealed that the lake was not ice covered during the Last Glacial Period (Colhoun et al., 1999).

3. Material and methods

3.1. Coring and sampling

Coring of Lake Selina was completed in November 2014 from a floating platform rigged on two inflatable rafts. Two sites were cored from the approximate lake center (Fig. 1C). Three cores were recovered including a short gravity core LA (84 cm) and two Nesje (Nesje, 1992) cores N1 (sections A, B, C; 394 cm) and N2 (sections A, B, C, D; 497 cm) (Fig. 2A). The cores were transported to the University of Melbourne, stored in a cold room, and split using a GEOTEK core splitter. For each core section, one half was reserved for micro-XRF (ITRAX) core scanning and archiving, and the other half for multi-proxy sampling. The sampling strategy includes biogenic proxies (results reported elsewhere), radiocarbon dating, OSL dating, paleo- and rock-magnetism, and beryllium isotopes.

3.2. Micro-XRF core scanning

The cores were scanned using a micro X-ray fluorescence ITRAX core scanner at the Australian Nuclear Science and Technology Organisation (ANSTO). Optical and X-ray radiograph images of the split cores were acquired, and elemental composition was measured at 0.02 cm intervals. All measurements were conducted using a molybdenum (Mo) target tube set at 30 kV and 55 mA with a dwell time of 10 s. The pass-through radiation (RAD) is a proxy for density (Francus et al., 2015) and the ratio inc/coh is a proxy for sediment organic content (Woodward and Gadd, 2018). Principal component analysis (PCA) of the XRF core scanning data was performed to extract the main components of variance. The selected variables include elements with significant counts (>30 kcps),

RAD, inc/coh, and color RGB. Prior to PCA, each variable was scaled by subtracting the mean and normalising by the standard deviation.

3.3 Radiocarbon dating

Samples for radiocarbon dating were taken from core sections LA, N2-A and N2-B (Fig. 2A). Supplementary Material 1 includes core photographs and radiocarbon samples position. A total of 29 bulk sediment samples of 0.5 cm thickness were analysed at DirectAMS Radiocarbon Dating Service laboratory. The radiocarbon ages are calibrated using the Southern Hemisphere calibration curve ShCal20 (Hogg et al., 2020).

3.4 Optically stimulated luminescence (OSL) dating

Twenty-three samples for OSL dating (OSL samples) and an additional 21 from above, between and below each OSL sample for field moisture content and environmental dose rate measurements (DOS samples), were collected from core sections N1-A, N1-B, N1-C, and N2-D (Fig. 2 and Sup. Mat. 1). Samples were 3-7 cm thick and collected from clastic sediment facies. Quartz grains (90-125 µm diameter) were isolated for OSL dating, purified using standard procedures (e.g. Wintle, 1997) and measured on an automated Risø TL-DA-20 luminescence reader (Bøtter-Jensen et al., 2003).

Equivalent dose (De) values were estimated from 6–10 multi-grain aliquots (~300 grains per aliquot) for each sample using the single aliquot regenerative-dose (SAR) procedure (Wintle and Murray, 2000). Aliquots were preheated at 240°C for 10 s prior to optical stimulation with blue LEDs for 40 s at 125°C prior to measurement of the natural (Ln) and regenerative doses (Lx). A fixed test dose (~5.4 Gy, also preheated at 240°C for 5 s) was applied after each Ln and Lx and the induced OSL signals (Tn and Tx) measured. Also included were duplicate and zero regenerative dose cycles and an OSL-IR depletion ratio test. Sensitivity-corrected (Lx/Tx) dose response curves (DRCs) were then constructed from the Lx and Tx OSL signals, using a saturating exponential function, and the sensitivity-corrected natural OSL signal (Ln/Tn) projected onto the fitted DRC to estimate De by interpolation.

Choice of measurement parameters were tested using a series of dose recovery tests (Galbraith et al., 1999). Aliquots of sample OSL5 (N = 21) were measured using seven different preheat combinations (180/180, 260/160, 180/160, 200/200, 220/220, 240/220 and 240/240) and a given dose of ~80 Gy. Accurate measured/given dose ratios were only obtained for two combinations: 240°C for 10 s (PH-1) and 240°C for 5 s (PH-2) (mean = 1.01 ± 0.07; N = 3) and 220°C for 10 s (PH-1) and 220°C for 5 s (PH-2) (mean = 1.00 ± 0.06, N = 3).

Environmental dose rates were calculated as the sum of the beta, gamma and cosmic-ray dose rates external to the grains, plus a small alpha dose rate from inside the quartz grains (0.03 ± 0.01 Gy/ka). We assumed that present-day radionuclide activities and dose rates have prevailed throughout the period of sample burial. Gamma dose rates were estimated from uranium, thorium and potassium concentrations obtained from a combination of inductively coupled plasma mass spectrometry (ICP-MS) and optical emission spectroscopy (ICP-OES) and converted to gamma dose rates using the conversion factors of Guérin et al. (2011). Beta dose rates were estimated from GM-25-5 beta counting using the procedures described and tested previously (Jacobs and Roberts, 2015), including a correction for grain size (Brennan, 2003). Cosmic-ray dose rates were calculated following Prescott and Hutton (1994), adjusting for site altitude, geomagnetic latitude, and the density (1.8 g/cm^3 for sediment and 1.025 g/cm^3 for water) and thickness of sediment overburden and an average

permanent water depth of 5 m. Beta, gamma and cosmic-ray dose rates were corrected for a moisture content of 40 ± 10% for all samples (Nathan and Mauz, 2008). The De divided by the environmental dose rate gives the burial time of the grains in calendar years ago.

3.5 Magnetic analysis

Paleomagnetic 8 cm^3 cube samples were taken continuously from cores LA, N1-A, N1-B, N1-C, N2-C, and N2-D (Fig. 2A). Core N2-A (24-81.6 cm section depth) was sampled for duplicate measurements. A total of 287 cube samples and 24 discrete samples (1 g) were analysed at the Australian National University. Magnetic analyses of the cube samples include low field volumetric magnetic susceptibility (klf) measured with an AGICO Kappabridge, and the natural, anhysteretic, and isothermal remanent magnetizations (NRM, ARM, and IRM, respectively) measured with a 2G cryogenic magnetometer. The NRM was demagnetized in 13 steps to maximum alternating field (AF) of 90 mT. The results were analysed in Puffinplot (Lurcock and Wilson, 2012) using unanchored principal component analysis (PCA). The cores were not azimuthally oriented; the declination records are aligned by subtracting the average declination of the non-anomalous values from each section. The ARM was induced using a direct current field of 0.05 mT and peak AF of 100 mT and demagnetized in 7 AF steps. A first IRM was induced in 1 T field using a 2G pulse magnetizer and demagnetized in 6 AF steps, and a second IRM was induced in 0.3 T field in the opposite direction and measured. Useful coercivity indicators from the remanence measurements include the median destructive field (MDF; the field required to demagnetize half the initial remanence; Dankers, 1981), the ARM ratio (kARM/IRM; Peters and Dekkers, 2003), the S-ratio ($IRM_{-0.3T}/IRM_{1T}$; a proxy for the relative contributions of low and high coercivity minerals to the total IRM; Liu et al., 2012) and the HIRM ($(IRM_{1T} + IRM_{-0.3T})/2$; the absolute contribution of high coercivity minerals to the total IRM; Liu et al., 2012).

Magnetic analyses of the 24 discrete samples were used to further characterise the magnetic mineral assemblage. The analyses include hysteresis loops, IRM acquisition and back field curves using a Princeton Measurements Corperation Vibrating Sample Magnetometer (VSM). The remanence ratio (saturation remanence (Mrs)/saturation magnetisation(Ms)) and the coercivity ratio (the remanent coercive force (Hcr)/bulk coercive force (Hc)) calculated from hysteresis loop and back field curve data are useful magnetic grain size and mineralogy indicators (Peters and Thompson, 1998; Roberts et al., 2011). IRM acquisition curves were analysed using MAX UnMix (Maxbauer et al., 2016). First-order reversal curves were acquired on 4 samples and processed using FORCinel (Harrison and Feinberg, 2008) with VARIFORC smoothing (Egli, 2013). Thermomagnetic curves were acquired for the representative samples N1-A18 and N1-C37. High-temperature cycling of magnetic susceptibility was measured from room temperature to 700 °C using a AGICO MFK2, and low-temperature cycling of room-temperature saturation isothermal remanent magnetisation (RTSIRM 5T) was measured down to 10 K using a Quantum Design Magnetic Property Measurement System (MPMS) at the Australian National University.

3.6 Beryllium isotopes analysis

Samples for beryllium isotope analysis were taken from core sections N1-A and N1-B (Fig. 2A) on one side of the trench left by paleomagnetic cube sampling at corresponding depth intervals. A total of 45 samples were analysed at CEREGE National Cosmogenic Nuclides Laboratory following the method established by Bourlès et al. (1989) and revised by Simon et al. (2016b). Authigenic ^{10}Be and its stable isotope ^{9}Be were extracted from ~1 g dry sample by soaking the samples in 20 ml of

leaching solution (0.04 M hydroxylamine (NH2OH–HCl) and 25% acetic acid) at 95 ± 5°C for 7 h. A 2-ml aliquot of the resulting leaching solution was sampled for measurement of the natural ^{9}Be concentration using a graphite-furnace atomic absorption spectrophotometer (AAS) with a double beam correction (Thermo Scientific ICE 3400). The remaining solution was spiked with 300 µl of a 9.8039 × $10^{-4}g^{-1}$ ^{9}Be carrier before Be purification by chromatography to determine accurate ^{10}Be sample concentrations from accelerator mass spectrometer (AMS) measurements of ^{10}Be /^{9}Be ratios. ^{10}Be sample concentrations were calculated from the measured spiked ^{10}Be /^{9}Be ratios normalised to the BeO STD-11 in-house standard (1.191 ± 0.013 × 10^{-11}) (Braucher et al., 2015). Authigenic 10Be concentrations were decay-corrected using the ^{10}Be half-life ($T_{1/2}$) of 1.387 ± 0.012 Ma (Chmeleff et al., 2010; Korschinek et al., 2010) and the dipole-independent age model (see below).

3.7 Core correlation

Core correlation is based on 24 visible stratigraphic tie-points and one inc/coh data tie-point (Fig. 2A). The correlation of the gravity core (LA) to the Nesje cores (N1 and N2) is set using a large amplitude change in inc/coh ratio at 75 cm in LA, 29 cm in N1-A, and 25 cm in N2-A (Fig. 2B). The inc/coh correlation depths correspond to the maximum inc/coh value after the inflection. The composite depth LAN2 is the reference record (Fig. 2C) used in this work. Data measured on samples from core N1 (OSL, beryllium, and magnetism) is transferred to the reference depth LAN2 using a transfer function based on linear interpolation and the 24 stratigraphic tie-points (Fig. 2A; cf. Result section 4.1 Lithology; Sup. Mat. 2). This assumes constant sedimentation rates between tie-points within each facies. We note that the stratigraphy of core section N2-A is potentially disturbed; a sediment gap formed (at 114 cm depth LAN2) during core splitting and two sub-sections were labelled (N2-A-a and -b; Fig. 2A). Thus, the duplicate magnetic data from core section N2-A is represented in the figures by points only.

4.Results

4.1. Lithology

Sediments from Lake Selina are characterised by two main facies, I and II (Fig. 3). These sedimentary facies have been associated with interglacial and glacial time intervals based on previous coring and radiocarbon dating (Colhoun et al., 1999). Interglacial facies I is homogeneous dark brown to black mud with lower density (RAD), higher organic content (inc/coh), lower ferrimagnetic content (klf, NRM, ARM, IRM) and lower bulk coercivity magnetic minerals assemblage (HIRM, S-ratio) than glacial facies II. Facies II is lighter in color, more clastic (higher Pb, Zn, Rb, Zr, Si, K) and composed of two main sub-facies (IIa and IIb) that alternate in distinct or mixed layers, sometimes including laminations. The sub-facies IIa is grey-beige mud and has the lowest organic content, the highest ferrimagnetic content and the higher magnetic coercivity assemblage. Sub-facies IIb is grey-brown mud with occasional lighter mud clasts and intermediate values between facies I and facies IIa. A few pebbles were found during sub-sampling (Fig. 2). Figure 4 illustrates the XRF PCA variables contribution to the principal components PC1 and PC2. The organic matter proxies (inc/coh, RAD, Br) and the elements associated with the clastic fraction of the sediment and the local geology (Rb, Zr, Si, Pb, Zn, K) strongly influence PC1 and are negatively correlated.

Cores N1 and N2 have the same stratigraphic sequence and are readily correlated visually (Fig. 2). However, some of the facies in N1 and N2 have different thickness (discussed in section 5.1). The

297 average facies difference is 1.7 cm thicker in N1 and the most outstanding example is the uppermost
298 glacial clastic facies IIa that has a thickness of 1 cm in N2 and 7 cm in N1. Yet, the facies alternation
299 provides 24 unambiguous stratigraphic tie-points. The cumulative depth difference is an additional
300 35 cm in composite depth LAN1 compared to LAN2 at the deepest tie-point (431 cm depth LAN1 and
301 396 cm depth LAN2; Fig. 2; Sup. Mat. 2). There is a series of oblique contacts and a cm-sized dark
302 vertical stain (organic debris) near the base of the core in the lowermost facies II (516-544 cm depth
303 LAN2).

304

305 ## 4.2. Radiometric dating (^{14}C and OSL)

306 A total of 29 ^{14}C (Table 1) and 12 OSL ages (Table 2) were obtained from the TAS1402 cores. The
307 oldest age is 84 ± 5 ka at 174.5 ± 2.5 cm depth LAN2 (OSL13; Table 2). OSL signals for samples
308 collected below this depth (OSL14 to 23) were in dose saturation, so finite De values and ages could
309 not be obtained. Most samples have overdispersion values <20% (Table 2), consistent with samples
310 that were well-bleached prior to deposition and remained largely undisturbed. The radial plots show
311 tight distributions of De values, in which the majority lie within ± 2 standardised estimates of a
312 common value (Sup. Mat. 3). The weighted mean De values for age determination were calculated
313 using the central age model (CAM) of Galbraith et al. (1999) (Table 2). The dose rate data are
314 provided in Table 2 and shown for all OSL and DOS samples between depths of 81 and 190 cm depth
315 LAN2 in Fig. 5. The total dose rates are similar for different samples, and there are no significant
316 trends with depth or between different sediment facies. A comparison of beta dose rates
317 determined using two independent methods and laboratories verify the reliability of the beta dose
318 rate measurements (Fig. 5D). The final optical ages are presented in Table 2. Uncertainties on the
319 ages are given at 1σ (the standard error on the mean) and were estimated by combining, in
320 quadrature, all known and estimated sources of random and systematic error.

321 Figure 6 presents the radiometric dating results and Bayesian age-depth model (rbacon; Blaauw and
322 Christen, 2011). The OSL ages (ka before 2018) were corrected by 68 years to make it equivalent to
323 the calibrated radiocarbon ages (ka before 1950 – ka cal BP). ^{14}C and OSL samples overlap over the
324 interval 83–177 cm LAN2 depth. Below the first OSL-dated clastic sediment sample at 83−84 cm
325 LAN2 depth, the calibrated ^{14}C ages return age inversions with apparently too 'old' and too 'young'
326 ages relative to OSL. Calibrated ^{14}C ages reach a plateau at ca. 40 ka cal BP (grey symbols in figure 6).
327 The two calibrated ^{14}C ages (D-AMS 027826 and D-AMS 015350; Table 1) that appear too 'old' may
328 indicate older organic material input to the coring site. The calibrated ^{14}C ages that appear too
329 'young' can be explained by two processes. First, underestimation of ^{14}C ages by modern carbon
330 contamination (Fig. 6B; Pigati et al., 2007). Contamination has greater impact on older materials (>35
331 ka BP) that contain proportionally less radiocarbon than younger materials. Figure 6B shows that
332 true ^{14}C ages >40 ka BP with 1-2% modern carbon contamination always returns ^{14}C ages of about
333 30–35 ka (32–38 ka cal BP). This likely explains the vertical distribution of 7 calibrated ^{14}C ages below
334 ~110 cm, where 4 other samples returned results not distinguishable from background (NDFB; Table
335 1, Fig. 6). Second, percolation of carbon down the core through the porous glacial lithologies (e.g.
336 Briant and Bateman, 2009; Long and Shen, 2014). This process may explain ^{14}C ages younger than
337 OSL and <35 ka (D-AMS 027827, D-AMS 027828, D-AMS 009084; Table 1). Unlike modern carbon
338 contamination, the migration of young carbon in sediments is site-specific and difficult to quantify. It
339 is, however, limited by the stratigraphy because percolation takes place through porous material at
340 a lithological boundary. Thus, we can reasonably assume that young carbon migration only affects
341 ^{14}C ages at depths greater than the uppermost porous detrital layer (>83 cm LA-N2 composite
342 depth).

To investigate further the young carbon effect, we compare two Bayesian age modeling runs (rbacon; Blaauw and Christen, 2011): the first using all calibrated ^{14}C and OSL ages (run 1) and the second using only the 12 calibrated ^{14}C ages from 0–83 cm and all OSL ages (run 2). With run 2, we assume that the ^{14}C ages at depths >83 cm are affected by old or young carbon contamination, and/or downcore percolation, all of which relate to lithological changes during the Last Glacial Period. Run 1 and 2 return quite similar age-depth models, however run 1 shows sharper changes in sedimentation rate constrained by the extra ^{14}C ages at depths >83 cm. Key to this exercise is that rbacon independently rejected the too 'old' and too 'young' ^{14}C ages as hypothesized from the lithology, providing support to the run 2 sample selection (Sup. Mat. 4). We select the more conservative age-depth model run 2, based on 12 calibrated ^{14}C and 12 OSL ages, to avoid any bias induced by unknown young carbon migration and old/young carbon contamination. The inclusion of stratigraphic boundaries (Sup. Mat. 2) in the rbacon model to allow for sedimentation changes between facies returns the same result within uncertainty as model runs that do not include stratigraphic boundaries (Sup. Mat. 4). The age-depth model run 2 based on radiometric dating is hereafter referred to as "Radiometric".

4.3. Magnetic mineral assemblage

Ferrimagnetic mineral content varies by up to one order of magnitude between sediment facies I and II (Fig. 3; klf, NRM, IRM). The organic-rich facies I has weak average NRMs of 2 $x10^{-3}$ Am^{-1} and klf values of 7 $x10^{-6}$ SI. The more clastic facies II has average NRM and klf values five to ten times higher, of 21 $x10^{-3}$ Am^{-1} and 35 $x10^{-6}$ SI, respectively. Slightly coarser magnetic grains (kARM/IRM, MDF_{ARM}, Mr/Ms) and more high coercivity minerals (HIRM) characterize facies II compared to facies I (Fig. 3). The magnetic mineralogy is a mixed magnetic assemblage comprising at least two contrasting coercivity populations as indicated by wasp-waisted hysteresis loops (Fig. 7) and S-ratio varying between 0.4 and 0.8 (Fig. 3). The mineralogy discriminant remanence ratio ARM40mT/SARM (Peters and Thompson, 1998) (Fig. 8) and the average Hcr/Hc value of 4.5 ± 1.5 indicate that magnetite is the primary remanence carrier (pyrrhotite and greigite have Hcr/Hc <1.5; Peters and Thompson, 1998; Roberts et al., 2011). Further magnetic mineralogical evidence comes from the temperature-dependant analysis. The low temperature analyses do not reveal a magnetite Verwey transition (a change in remanence at 120 K) and the RTSIRM curve is almost reversible (Fig. 7B and F), which is typical of surficially oxidized magnetite (maghemite), titanomagnetite, and/or goethite as remanence carriers (France and Oldfield, 2000; Lacroix and Guyodo, 2017). The goethite Curie temperature (120 °C) is occasionally seen in the thermomagnetic curves of magnetic susceptibility for facies II samples. None of the (not shown). No thermomagnetic curves are reversible and ferrimagnetic minerals are formed and/or grain size changed from about 400 °C (Fig. 7B and F). Yet, t his transformation is not diagnostic and may result from heating of other iron oxides, iron sulphides, hydroxides, carbonates or silicates originally present in the sediments (Henry, 2007). Finally, five samples from facies II (<2% of the samples) acquired a gyroremanent magnetisation (GRM) during stepwise AF demagnetisation of the NRM in fields >40 mT, indicating presence of some greigite in the lake sediments (e.g., Roberts et al., 2011; Lise-Pronovost et al., 2014).

Unmixing of the 24 IRM acquisition curves using MAX UnMix (Maxbauer et al., 2016) indicates a minimum of three subpopulations of magnetic mineral particles (P1, P2, P3) with average coercivity ranges <20 mT (P1), of 63 ± 9 mT (P2), and >270 mT (P3) (Fig. 7). The lower coercivity population P1 may correspond to multidomain particles with an average estimated contribution to the IRM of 10 % (Maxbauer et al., 2016). The high coercivity population P3 has an average estimated contribution to the IRM of 40 % and may correspond to hematite and/or goethite (Egli, 2004). The dominant

population is P2 with an estimated contribution of 50 % to the IRM and a medium coercivity range that corresponds to fine iron oxide particles (Egli, 2004). While the P2 range of IRM unmixed coercivities better match biogenic magnetite, the MDF_{ARM} values (20–30 mT), ARM ratio (0.38 mmA^{-1}), and dispersion parameter value (log DP_{P2} = 0.4) closely match the typical values for detrital, pedogenic, extracellular, or aeolian sources (Egli, 2004; Maxbauer, 2016). Further support for a non-biogenic source is provided by the FORC diagrams (Fig. 7F) which indicate vortex and interacting single domain particles (Harrison et al., 2018) based on the absence of a central ridge feature associated with the non-interacting single domain particles, typical of biogenic magnetite (Egli et al., 2010; Heslop et al., 2014). Yet, it is unclear if P2 has a detrital and/or biogenic origin, as biogenic magnetite may have oxidized to maghemite. We note that a dual biogenic and detrital origin for the iron minerals would be consistent with Fe being neutral in the PC1 opposing organic and clastic variables (Fig. 4). The proportion of the primary magnetic population P2 is maximum in facies II and accounts for the higher ferrimagnetic concentration (klf, NRM, ARM, IRM; Fig. 3). In summary, the magnetic analysis results indicate a principal magnetic population of oxidized detrital (titano-) magnetite (P2) present throughout all sedimentary facies (Fig. 7) and isolated by alternating field demagnetisation of the ARM and IRM (Fig. 8). Up to half the estimated contributions are attributed to combined secondary populations of low coercivity ferrimagnetic material (P1) and high coercivity hematite and/or goethite (P3).

4.4. Paleomagnetic record

4.4.1. Paleomagnetic directions

The paleomagnetic directions calculated for all demagnetisation steps (13 steps from 0 to 90 mT) show inclinations varying near the expected value (-61°) for the site latitude and a geocentric axial dipole (GAD). However, the inclination and declination demagnetisation data are noisy with maximum angular deviation (MAD) reaching values up to 40° (Fig. 9A). The MAD is approximately inversely proportional to the NRM intensity, with highest MAD values in weakly magnetic interglacial sediments (facies I) and the most stable directions in glacial sediments (facies II). There is no evidence of inclination shallowing or paleomagnetic directional (in)stability tied to specific facies. Overlapping core sections LA, N1-A and N2-A give reproducible results (Fig. 9A). A two-step selection process was applied to select a paleomagnetic direction record (Fig. 9B). First, the optimum characteristic remanent magnetisation (ChRM) interval is selected for each sample. The demagnetisation steps associated with any viscous overprint (<20 mT), weak noisy values at higher fields and GRM (>40 mT) are left out. Most selected ChRM intervals lie between 10 and 60 mT and include about 9 demagnetisation steps. Second, we select samples having a minimum of 5 consecutive steps and MAD values <20°. 76 % of the samples pass these selection criteria and the selected paleomagnetic directions data are shown in figure 9B. The selected paleomagnetic directions demonstrate overall small-scale oscillations, in agreement with paleosecular variation, except for few intervals showing large-scale deviations (Fig. 9B). The distinction between secular variation and geomagnetic instabilities (e.g. geomagnetic excursions) is often defined empirically by a deviation of the virtual geomagnetic pole (VGP) by more than 45° accompanied by paleointensity minima (e.g. Roberts, 2008; Laj and Channell, 2015). Here, we consider that paleomagnetic inclinations departing >45° away from the GAD and associated with large amplitude changes in declination correspond to “excursional” events featuress (Fig. 9B). These “excursional” events features are found in the interval 91-116 cm depth LAN2 (facies IIa and IIb), at 302 cm depth LAN2 (facies I), and at 558 cm and 565 cm depth LAN2 (lowermost facies IIa).

435 4.4.2. Relative paleointensity (RPI)

436 RPI is estimated by normalising the NRM with a rock-magnetic parameter such as the ARM or IRM to
437 isolate the geomagnetic signal, considered to be proportional to the ancient field intensity, from the
438 concentration of the remanence carrying ferrimagnetic mineral. A set of criteria for rock magnetic
439 homogeneity is traditionally used to assess the quality of sediments for RPI reconstruction (King et
440 al., 1983; Roberts et al., 2013). 1) The ferrimagnetic concentration should vary by less than one
441 order of magnitude (klf, ARM, IRM), 2) the ideal magnetic mineral is magnetite, and 3) the ideal
442 magnetic particle size is single domain (SD). The magnetic mineralogy results indicate that the
443 sediments from Lake Selina barely fulfill these criteria (Figures 3, 7, and 8). The ferrimagnetic
444 content of facies I and II differs by one order of magnitude and although fine magnetite particles (P2)
445 dominate the magnetic mineral assemblage, magnetite is not the only ferrimagnetic mineral.
446 Downcore homogeneity of the magnetic mineral assemblage is crucial for RPI reconstruction
447 because different magnetic particles can have different recording efficiencies that are difficult to
448 reconcile into a continuous RPI record (e.g. Chen et al., 2017). Figures 9C and D compares four RPI
449 estimates. The raw data in Figure 9C illustrates efficiency differences in the sediments of Lake Selina,
450 with RPI values varying over one order of magnitude. Data deemed unsuitable for RPI include
451 isolated peak RPI values up to 5 reflecting NRM overprint (Fig. 9C) and high $NRM_{20\ mT}$ /$ARM_{20\ mT}$
452 values >0.4 corresponding to high MDF_{NRM} values >30 mT (not shown). These intervals have a
453 distinct remanence efficiency apparently associated with some of the facies IIa; they are highlighted
454 in grey in figures 3 and 9. Figure 10D presents the selected RPI estimates (without data from the grey
455 intervals). The RPI estimates include NRM normalisation by ARM and IRM at 20 mT demagnetisation
456 (NRM_{20mT}/ARM_{20mT} and NRM_{20mT}/IRM_{20mT}) and by the portion of remanence removed between 10
457 mT and 60 mT demagnetisation ($NRM_{10\text{-}60mT}$/$ARM_{10\text{-}60mT}$, $NRM_{10\text{-}60mT}$/$IRM_{10\text{-}60mT}$) to specifically target
458 the P2 magnetic population. The four RPI proxies are similar (Fig. 9C-D), which supports P2 as the
459 main remanence carrier isolated in laboratory AF fields. The interval 10-60 mT has the best
460 reproducibility between cores (LA, N1 and N2 overlap; Fig. 9D) and therefore $NRM_{10\text{-}60mT}$/$ARM_{10\text{-}60mT}$
461 is selected as the preferred RPI estimate. In the interval displaying excursional directions, eight RPI
462 data (3 cubes from core N1 and 5 cubes from N2) did not pass the selection criteria because of their
463 different remanence efficiency. A total of six samples (3 cubes from core N1 and 3 cubes from N2)
464 have both reliable RPI and excursional directions, including the low RPI interval from 110 to 116 cm
465 depth LAN2 (Fig. 10).

466

467 4.4.3. Beryllium isotopes

468 The authigenic 9Be concentrations range from 0.1 to 2.2 x1016 $at.g^{-1}$, with an average value of 0.6 ±
469 0.4 $x10^{16}$ $at.g^{-1}$ (Fig. 3). The authigenic ^{10}Be (decay-corrected) concentrations range from 3.1 to 36.7
470 $x10^{8}$ $at.g^{-1}$, with an average value of 12.6 ± 7.1 $x10^{8}$ $at.g^{-1}$. These ^{10}Be and ^{9}Be concentrations and
471 variation ranges are larger than those found in most marine records (e.g. Simon et al., 2016a and
472 references therein) or existing lacustrine sediments (e.g. Horiuchi et al.., 2001; Czymzik et al., 2015;
473 Du et al., 2018; Tang et al., 2019), except from the closest lacustrine record (i.e. Lake Pupuke in New
474 Zealand; Nilsson et al., 2011). Such large-scale concentration variations indicate large changes of Be
475 inputs into the lake controlled by transport and deposition processes, but not associated with ^{10}Be
476 production rates (e.g. Simon et al., 2016b). The fact that both ^{9}Be and ^{10}Be concentrations vary
477 similarly (correlation coefficient r=0.97; Sup. Mat. 5) and display two peak intervals also found in
478 elemental ratios (e.g. Pb/Al) and magnetic properties (e.g. magnetic susceptibility, HIRM) associated
479 with local runoff (Fig. 3), suggests that ^{9}Be and ^{10}Be have the same transport pathway to the lake as
480 clastic detrital particles.

The ^{10}Be is used for reconstructing geomagnetic dipole moment variations by normalising ^{10}Be concentration by its stable isotope ^{9}Be (hereinafter Be ratio) to try minimizing environmental influences (Bourlès et al., 1989). The Be ratio varies from 14.7 x10^{-8} to 23.7 x10^{-8}, with an average of 20.7 ± 2.3 x10^{-8}. One single Be ratio peak reaching 28 ± 1.0 x10^{-8} at 95 cm depth LAN2 was identified in a first batch, but not reproduced by a replicate measurement (Table 3). Excluding this measurement outlier, the highest Be ratio values (>22 x10^{-8}) are found in the intervals 91–95 cm and 110–117 cm depth LAN2. The latter interval is coeval with the RPI low and excursional paleomagnetic inclinations (Fig. 10). In the top 90 cm of the core (Holocene facies I), the Be ratio decreases significantly and reaches its lowest values (<18 x 10-8). These low Be ratio values are explained by a dilution of ^{10}Be inputs between the Holocene interval and the Last Glacial Period (Willenbring and von Blanckenburg, 2010; Sup. Mat. 5). This is likely associated with large-scale atmospheric reorganization and environmental change within the lake watershed since the last glacial to interglacial climate transition (Fig. 3) and higher sedimentation rates. Excluding these Holocene results, Be ratio and RPI have a correlation coefficient of r=-0.36, and r=-0.5 for the grey shading interval of figure 10. Considering the large lithological changes observed during the Last Glacial Period, these moderately good correlations may relate to unaccounted for environmental biases on both geomagnetic field intensity proxies and/or to unknown lock-in-depth affecting the RPI (Roberts and Winklhofer, 2004; Nilsson et al., 2018; Simon et al., 2018, 2020b). The phasing between RPI low and Be ratio peak between 110–117 cm depth LAN2 suggests a very limited lock-in depth, but data resolution and lithological changes prevent any strong inference.

5. Discussion

5.1 Depositional processes in Lake Selina and instability of the Last Glacial Period

The difference in facies thickness between the two cores could point to event deposits as suggested by the occasional mm-sized pebbles in facies IIa (black lozenge on Fig. 2 stratigraphic logs). However, a pebble is also found in facies I and there are no clear and systematic geochemical, magnetic, and physical evidence for event deposits as reported elsewhere in lakes, fjords and harbour sediments (e.g. St-Onge et al., 2004; Guyard et al., 2007; Lisé-Pronovost et al., 2014; 2019b). No basal erosive contacts are observed and the base of facies units contains no vegetal debris, nor present any systematically higher density (RAD; Fig. 3), higher concentration of ferrimagnetic minerals (ARM, IRM; Fig. 3), or abnormally shallow paleomagnetic inclinations as would be expected for instantaneous event deposits such as floods, extreme precipitation or melt runoff. The facies IIa from lowermost part of core N2 (516-544 cm depth LAN2) is the only one standing out as a likely event or disturbed deposit because it has oblique structures (visible in the radiograph and photo, Sup. Mat. 1), a 3-cm vertical black stain, pebbles, flattened inclinations and sharp large amplitude changes in magnetic grain size proxies (kARM/IRM and MDF_{ARM}; Fig. 3). All other facies I, IIa and IIb are interpreted as distinct types of normal lake sediment deposits and the pebbles are assumed to have reached the coring sites through a process independent of facies type (e.g. isolated meteorological event). The difference in facies thickness between cores can alternatively be attributed to the coring site N1 being closer than N2 to gullies from Lake Westwood to Lake Selina (Fig. 1C). This is supported by glacial facies (IIa and IIb) being on average 1.6 times thicker in N1 than N2 (N1/N2) and coarser magnetic particles deposited at coring site N1 than N2 (kARM/IRM and MDF_{ARM} data of overlapping sections N2-A; Fig. 3). Detrital input from the gullies likely also accounts for the southwest of Lake Selina being filled in the modern wetland (Fig. 1C). Future geophysical surveys will be useful to find out the total sediment thickness accumulated in Lake Selina.

The Last Glacial Period (MIS 2, 3 and 4) also stands out as more unstable than the previous glacial period (MIS 6), with greater and more variable facies thickness differences between cores (N1/N2 ratio of facies thicknesses are 1.82 ± 1.68 for the Last Glacial Period and 1.17 ± 0.16 for MIS 6). The relatively unstable stratigraphy of the Last Glacial Period may be linked to climate and/or human influence on the transport of clastic sediments to the lake. The distinct climatic signal of the two last glacial periods in the Lake Selina data may be attributed to their different orbital configurations (e.g. Ruddiman, 2006) and the global distribution of continental ice (Rohling et al., 2017). Distinct regional climate signals for the two last glacials are similarly reported elsewhere (e.g. de Abreu, 2003, Fritz et al., 2004; Roucoux et al., 2011). While MIS 6 is poorly documented in the Australian region, dramatic climate changes are documented for the Last Glacial Period in the marine and continental temperate regions of Australia, from cold MIS 4 (de Deckker et al., 2019) to wet MIS 3, and cold and arid MIS 2 (Fletcher and Thomas, 2010; Bostock et al., 2013; Falster et al., 2018; Kemp et al., 2019; Sniderman et al., 2019). Lake Mungo, in the Willandra Lakes system on mainland Australia (900 km north from Lake Selina), was permanent during MIS 4 and 2 and underwent large-scale oscillating lake levels during MIS 3 (Fitzsimmons et al., 2015). At Lake Selina, the frequent alternation of the more clastic facies IIa and the more organic facies IIb may suggest similar lake level fluctuations with changing conditions controlled by an on/off type of control. Examples of on/off switches include temperatures near freezing point and the hydrological connection from Lake Westwood to Lake Selina. Gullies may have only been active at temperatures above the freezing point at the altitude of Lake Westwood, less active during arid periods (e.g. MIS 2), and much more active in wet climate (e.g. wet MIS 3; Falster et al., 2018; Kemp et al., 2019). While there is no evidence for ice cover on lakes Selina and Westwood, a sedimentary hiatus in the highest altitude Lake Julia (616 m asl) (Fig. 1C) suggests it was permanently ice-covered during MIS 2 (M.-S. Fletcher unpublished data). In addition to climate, the second non-exclusive hypothesis for the unstable signal of the Last Glacial Period is Indigenous land use practices such as vegetation burning in the lake catchment that would have impacted the availability of clastic material for erosion, since humans have occupied Tasmania for the last 43,000 years (Kiernan et al., 1983; Cosgrove, 1999). These hypotheses on the conditions controlling the depositional types will be addressed elsewhere using multi-proxy biotic and abiotic investigations from Lake Selina and Lake Westwood.

5.2 Radiometric dating

The heterogeneous lithology of the Last Glacial Period in Lake Selina is problematic for radiocarbon dating (Fig. 6). Downcore movement of humic acid and contamination has previously been reported at Lake Selina by Colhoun et al. (1999), precluding the determination of reliable sedimentation rates. The Radiometric age model obtained here by combining radiocarbon and OSL ages indicates an average sedimentation rate of 1.5 cm/ka for the Last Glacial Period (MIS 2, 3, 4) and 5.3 cm/ka for the uppermost facies I (MIS 1) (Fig. 6; Table 4). The average uncertainty of the radiocarbon and OSL-dated intervals is 0.8 ± 0.4 ka and is 8.2 ± 1.9 ka at 2σ, respectively. The OSL dating uncertainty and low sedimentation rates at Lake Selina prevent resolving any difference in accumulation rates between the glacial facies IIa and IIb.

MIS 2 is arguably the best dated interval of the Last Glacial Period because it is bracketed by the precisely radiocarbon-dated Holocene and a stratigraphic change from facies IIa to IIb dated at 30 ka BP (27,361−33,758 cal BP; Radiometric age model) in agreement with the accepted MIS 3/2 global boundary (29 ka; Lisiecki and Raymo, 2005). The Radiometric age model indicates that the uppermost facies IIb accumulated during MIS 2, the coldest period of the Last Glacial Cycle and a presumably arid period in the southeast of mainland Australia (Falster et al., 2018). In contrast, MIS

3 includes a series of clastic facies IIa interbedded with facies IIb. This stratigraphy may be linked to wetter conditions influenced by Southern Westerly Winds during MIS 3 (Kemp et al., 2019), with increased runoff episodes capable of transporting more detrital particles to the lake. A local source for the detrital material is supported by the magnetic, beryllium, and elemental data (Fig. 3). The magnetic assemblage has a detrital signature, with the same magnetic subpopulations present throughout sediment facies (Fig. 7), and the elemental composition is closely tied to the local geology (e.g. Pb/Al maxima in facies IIa; Fig. 3). The interpretation of these depositional processes inferred from the lithology and environmental magnetism results therefore concur to known climate variability in southeast Australia since MIS 4 using the radiometric age model. Radiometric dating in Lake Selina sediments is however limited to the uppermost 1.74 m (ca. 80 ka; Fig. 6).

5.3 Dating the full record with climate comparison

The environmental sensitivity reflected by contrasting sediment facies in Lake Selina is a challenge for radiocarbon dating but can be an advantage for climate-based relative dating. To explore this idea, we use Match dynamic programming (Lisiecki and Lisiecki, 2002) to synchronize climate proxies from Lake Selina with well-dated Antarctic ice core climate records. This is based on the assumption of linked millennial-scale climate in Antarctica and Tasmania, as documented in paleo-records from the Southern Hemisphere mid-latitudes (e.g. Pahnke, 2003; Barrows et al., 2007; Pugh et al., 2009; Fletcher and Moreno, 2012; Petherick et al., 2013; Abram et al., 2014) and the modern Southern Annular Mode (Garreaud, 2007; Hendon et al., 2007). Fletcher and Thomas (2010) further use a pollen transfer function to estimate temperature change from the Colhoun et al. (1999) pollen record from Lake Selina, identifying a tight coherence between Antarctic and Tasmanian temperature changes over the Last Glacial Cycle. This coherence supports our assumption of strong correlation between Tasmanian and Antarctic climatic variations.

Dynamic programming allows time series compression and expansion to account for varying sedimentation rates between compared natural archives, e.g. ice accumulates faster in cold glacial climates in Antarctica, while lake sediment accumulates faster during warm interglacial climates in Tasmania. The method is most efficient for large amplitude changes such as glacial/interglacial climate transitions. Taking this into account, the proxy data are selected based on their superficial similarity and six tie-points located at large amplitude changes are chosen (Fig. 11A). We use a double approach matching concurrently a) the inc/coh organic matter proxy from Lake Selina (Fig. 1) to the dD temperature proxy from EPICA Dome C (EDC; Jouzel et al., 2007; Fig. 11A) and b) the Pb/Al local runoff proxy from Lake Selina (Fig. 1) to the EDC dust flux (Lambert et al., 2012; Fig. 11B). The Southern Hemisphere atmospheric circulation links these proxies, with increased winds over the continental masses generating more atmospheric dust and more rainfall in western Tasmania (Fig. 1A and B). The Match-Climate age model is presented in Figure 12 and gives a basal sediment age of 266 ka. The average estimated sedimentation rates of Match-Climate are 5.2 cm/ka for interglacial facies I (MIS 5 and 7) and 2.6 cm/ka for glacial facies II (MIS 2, 3, 4, 6, and 8) (Table 4). These sedimentation rate estimates are similar to those using the Radiometric age model; however, the Match-Climate age model returns higher estimates for the Last Glacial Period.

Despite recognisable patterns of multi-millennial variability through glacial and interglacial climates, the low variance of climatic proxies over the interval 20−60 ka prevents any reliable visual matching in this interval (Fig. 11). The inc/coh comparison is poor over that period, with an R value of 0.25 compared to 0.84 for the entire record (Fig. 11). This compromises the applicability of Match-Climate age model over MIS 2-3. Providing there are no unidentified event deposits obscuring the

climate signal in the Lake Selina sequence, this mismatch may be linked to differences in regional climates in western Tasmania and in Antarctica over the Last Glacial Period, however, a close alignment between the climate of these regions is reported in the literature (Williams et al., 2009; Petherick et al., 2013; Kemp et al., 2019; Sniderman et al., 2019). Another possible explanation for the mismatch is a misinterpretation of the climate proxies. Additional local factors may influence one of the proxies in addition to the common climate forcing component. For instance, the ratio inc/coh in Lake Selina may not be solely controlled by atmospheric temperature. Therefore, the assumption that more organic sediments reflecting warmer temperatures does not hold for moderate variations, resulting in low R value during MIS 2–3. As discussed in section 5.1, precipitation and/or Aboriginal landscape management may have played a crucial role in the transport of clastic material to Lake Selina over the Last Glacial Period, thus decoupling the sedimentary record from climate through this interval of relatively small-scale climate fluctuations in the Antarctic record (when compared to the large orbital-scale glacial-interglacial oscillations).

5.4 Dating with paleomagnetism

5.4.1 Geomagnetic excursions

Up to 10 geomagnetic excursions have been recognised in the past 270 ka (Channell et al., 2020 and references therein). Of these, the Blake (120 ka), Laschamp (41 ka), and Mono Lake (32 ka) excursions are amongst the most globally documented from sedimentary and volcanic archives, but previously not from Australia. At Lake Selina, the interval 110–117 cm depth LAN2 is characterised by Be ratio maxima, RPI low, and excursional paleodirections associated with the Laschamp geomagnetic excursion (Fig. 10). While the dipole moment modulates the amount of beryllium isotopes ^{10}Be produced in the atmosphere, the total field intensity (dipolar and non-dipolar fields) can be recorded in sediments. Yet due to low sedimentation rates at Lake Selina, the RPI signal is likely to be dominated by dipolar variations only. Thus, the Be ratio and RPI records from Lake Selina are expected to vary similarly and are here referred to as geomagnetic field intensity proxies. The geomagnetic field intensity low attributed to the Laschamp has an estimated duration of about 5 ka based on the radiometric age model and the excursional directions interval extends over a longer period of about 10 ka. These durations are higher than the generally accepted < 2 ka for the Laschamp excursion (Channell et al., 2020). While this result may indicate undetected higher sedimentation rates in Lake Selina, a longer overall process duration for the Laschamp excursion was also reported from the closest available record, derived from volcanic rocks in New Zealand (Ingham et al., 2017). Korte et al. (2019) show that duration of the Laschamp can vary regionally depending on its definition and the model used. Such records of the Laschamp excursion in the Australasian region are therefore useful to document the non-uniform expression at the Earth's surface of a global phenomenon.

A second Be ratio maxima (91–95 cm depth LAN2, yellow highlight Fig. 10) does not correlate with an RPI low, but corresponds to a slight inclination shift above the GAD+45° limit and large amplitude declination change seen in N2 (however, not in N1). Thus, attributing this second event to a geomagnetic excursional feature seems speculative. We note however that its occurrence (from 26,632−32,747 cal BP to 23,812−29,041 cal BP; Radiometric age model) corresponds to a time period where geomagnetic intensity drops have been noted in different records, with the suggestion of two excursions at ca. 32 ka (e.g. Liddicoat and Coe, 1979; Lund et al., 2017) and ca. 26 ka (Channell et al., 2016). This timing also corresponds to a moderate Be ratio increase in core MD05-2930 from the Gulf of Papua, ca. 3500 km north of the Selina Lake (Simon et al., 2016a). Finally, one data point (302 cm depth LAN2) returning a paleomagnetic inclination departure >45° from the GAD together with

large declination variations and low RPI values during MIS 5e (Fig. 9D) correspond to the age of the Blake geomagnetic excursion (ca. 125 ka) according to the Match-Climate age model (Fig. 12). However, due to the high organic content and low ferrimagnetic content of the interglacial sediments (facies I; Fig. 3), the paleomagnetic directions are too poorly defined (Fig. 9) to confidently attribute these results to a geomagnetic excursion. Future beryllium isotopes analysis over this interval could be useful to test this interpretation, providing that Be ratio does not suffer from ^{10}Be dilution as during the Holocene facies I (see section 4.4.3).

5.4.2 Geomagnetic field intensity proxies

The best agreement of the two geomagnetic field intensity proxies (RPI and Be ratio) is found over the period 20−60 ka (80−140 cm depth LAN2; Fig. 10), the same interval where Match-Climate applicability is compromised (c.f. section 5.3). We use the Be ratio as our most reliable geomagnetic field intensity proxy for Match dynamic programming (Lisiecki and Lisiecki, 2002) because it is not affected by unknown lock-in delay and can be compared to the marine Be ratio stack of similar resolution (Simon et al., 2016a). The Match-Dipole age model covers the period 20−111 ka and falls within the Radiometric age model uncertainty for the period of overlap (Fig. 12). The average estimated sedimentation rate of Match-Dipole is 1.5 cm/ka for the Last Glacial Period facies II (MIS 2, 3, and 4), which is the same as the Radiometric age model estimate (Table 4). We note that running Match with the Lake Selina RPI data and other independent paleointensity references (GGF100k, Panovska et al., 2018; GLOPIS, Laj et al., 2014) returns similar results. Comparison of the Lake Selina geomagnetic field intensity proxies with the reference stack GLOPIS and the geomagnetic field model GGF100k (Fig. 13) illustrates that Match-Climate overestimates the age of the geomagnetic field intensity low associated with the Laschamp geomagnetic excursion (41 ka) by about 6 ka. Prior to 60 ka and back to 80 ka, the reference curves are not readily correlatable (Fig. 13; Laj et al., 2004; Simon et al., 2016a; Panovska et al., 2018), which may reflect dating difficulties in those records and limits the performance of Match dynamic programming.

5.5 Age models and uncertainties

There is an overall agreement within age uncertainties between all age models developed in this study, with an overlap of two to three age models (Radiometric, Match-dipole and Match-climate) for the interval between 81−223 cm depth LAN2 (Fig. 12). An average age model can be calculated for that interval, or more practically, the appropriate chronology can be selected for a given purpose, e.g. a climate-independent chronology for paleoclimate investigations (up to 111 ka), and a geomagnetic-independent chronology for paleomagnetic investigations (full record) (GEOMAGIA50, Brown et al., 2015; MagIc; https://www2.earthref.org/MagIC). Our preferred age model is the combination of Radiometric (0−70 ka) and Match-Climate (70−265 ka), independently supported by the Laschamp geomagnetic excursion. This choice is based on i) the Radiometric age model having age uncertainties encompassing Match-Dipole and most of Match-Climate age models (Fig. 12), and ii) Match-Climate being considered more reliable than Match-Dipole before 60 ka, where Be ratio and RPI are not synchronized (Fig. 10) and do not agree with other dipole reconstructions (Fig. 13). We select 70 ka as the transition point between our optimal age models (Fig. 12). For paleoclimate discussions, a second preferred age model is the combination of Radiometric (20−0 ka), Match-Dipole (20−70 or 111 ka) and Match-Climate (70 or 111−265 ka). This second option is aligned to global dipole millennial-scale variability and the Laschamp geomagnetic excursion (Fig. 13), and it is independent of climate over the longest possible period.

The overlap in independent age models during MIS 2−3−4 gives a means to estimate the uncertainty on ages obtained from the Match dynamic programming algorithm at Lake Selina. Match dynamic programming is deterministic; it gives one best solution and does not provide age uncertainties (Lisiecki and Lisiecki, 2002). Yet estimate of age uncertainty is desirable for the lowermost interval between 223-44 cm (111−265 ka) that only has one age model based on climate comparison (Fig. 12). The average age difference between the three overlapping chronologies is 4.4 ± 1.6 ka (Fig. 12 inset), which is smaller than the average uncertainty of the OSL-dated interval (8.2 ± 1.9 ka). We use the average deviation of the Match-Climate age to the other age models (Radiometric and Match-Dipole) over the interval where the three age models overlap to estimate the uncertainty on age of Match-Climate within the lowermost interval exclusively based on climate tuning. An estimated age uncertainty of 5.3 ± 2.3 ka is obtained. This age uncertainty estimate is comparable to the average age differences of 4.1 ± 2.8 ka between the Lake Selina stratigraphic transitions and the globally recognized MIS boundary ages (Lisiecki and Raymo, 2005) (Figure 12).

6. Conclusions

This work presents a chronostratigraphic model of Lake Selina core TAS1402, which is the oldest continuous continental archive in Tasmania. Radiometric dating (radiocarbon and OSL) and relative dating (paleomagnetism, authigenic ^{10}Be/9Be ratio and climate comparisons) were combined to construct a chronology extending to 266 ± 8 ka (MIS 8). The 5.5 m lake sediment archive is longer than the previously recovered 4 m core (Colhoun et al., 1999), and the sedimentation rate estimates are 5 cm/ka for interglacial periods and 1.5 cm/ka for glacial periods.

High-resolution XRF core scanning, beryllium isotopes and magnetic properties enable a matching of the sediment archive from Tasmania to ice core records of climate proxies in Antarctica. This agreement was used as a basis to date material beyond the range of radiometric methods (>80 ka) via a dynamic programming algorithm (Match; Lisiecki and Lisiecki, 2002). The interval 20−60 ka (MIS 2−3), however, returns poor correlations of climate proxies from Lake Selina to Antarctic records, in contrast to the rest of the record, and limits the application of climate comparison dating over that interval. We interpret the misfit to be caused by local controls, other than temperature, on the Lake Selina proxy inc/coh during a period of rapid climate oscillations and the arrival of humans in Tasmania (at ca. 43 ka). Paleomagnetic comparison over the interval 20−60 ka effectively constrains the chronology with geomagnetic field intensity proxies; authigenic ^{10}Be/^{9}Be ratio and relative paleointensity (RPI). The multi-method age modeling approach used here provided two preferred age models, nearly indiscernible within their uncertainties, which allows the use of a dipole-independent (270 ka to present) or a climate-independent age model (111 ka to present). The age uncertainties are lowest in the radiocarbon-dated uppermost 83 cm of the core (0.8 ± 0.4 ka) and are estimated to be within 8 ka for the entire sequence.

The period 45−35 ka (defined by the Radiometric age model) is a 14 cm interval that spans human arrival in Tasmania and the demise of the last remaining megafauna in this region. It has an average Radiometric age model uncertainty of 7.2 ± 0.4 ka and the average age difference for the three overlapping age models (Radiometric, Match-Climate, and Match-Dipole) is 2.5 ± 1.1 ka.

This work presents the first full-vector paleomagnetic record and environmental magnetism study in Tasmania. Despite a complex magnetic mineral assemblage with magnetic concentration changes up to one order of magnitude between glacial and interglacial sediment facies, the main paleomagnetic remanence carrier is detrital oxidised (titano)magnetite throughout all sediment facies. A set of

quality criteria were used to select the most reliable data. The paleomagnetic record from Lake Selina returns transitional paleomagnetic directions and low geomagnetic field intensity proxies (RPI and authigenic $^{10}Be/^{9}Be$ ratio) at the time of the Laschamp geomagnetic excursion. Comparison of the RPI and Be ratio with published virtual axial dipole moment reconstructions over the Last Glacial Period indicates negligible lock-in-depth and supports a genuine geomagnetic signal. Thus, providing a practical example for combining authigenic $^{10}Be/^{9}Be$ ratio and paleomagnetism to constrain the chronology of lake sediments.

7. Data availability

The data presented here will be available on PANGAEA: https://www.pangaea.de/. The paleomagnetic data will also be archived with the Magnetics Information Consortium (MagIC): http://earthref.org/MagIC/16529.

Acknowledgements

Thanks to the TAS1402 drilling team (Kristen K. Beck, Alexa Benson, Angelica Ramirez, William Rapuc, Anthony Romano) and the data science support team (Milan Korbel, Shashwat Pathak, Lachlan Simpson). This research was supported by use of the Nectar Research Cloud; a collaborative Australian research platform supported by the National Collaborative Research Infrastructure Strategy (NCRIS). We thank Maarten Blaauw for support with rbacon and Xiang Zhao and Andrew Roberts for assistance at the Paleomagnetism Laboratory at the Australian National University. This project was funded by the Australian Research Council Discovery Indigenous IN140100050 to M.-S. Fletcher and IN170100062 to M.-S. Fletcher and A. Lisé-Pronovost. A. Lisé-Pronovost was supported by a La Trobe University DVCR Fellowship and a University of Melbourne McKenzie Fellowship. D. Heslop was supported by the Australian Research Council (DP190100874). The ASTER AMS national facility (CEREGE, Aix en Provence) is supported by INSU/CNRS, ANR through the EQUIPEX "ASTER-CEREGE" action, and IRD.

References

Abram, N, Mulvaney, R, Vimeux, F et al. 2014, Evolution of the Southern Annular Mode during the past millennium, Nature Climate Change 4 (7), 564-569.

Aitken, M.J., 1985. Thermoluminescence Dating. Academic Press, London.

Aitken, M.J., 1998. An Introduction to Optical Dating. Oxford University Press, Oxford.

Anker, S. A., Colhoun, E. A., Barton, C. E., Petersen, M., Barbetti, M., 2001. Holocene vegetation and paleoclimatic and Paleomagnetic history from Lake Johnston, Tasmania. Quatern. Res. 56, 264–274. doi: 10.1006/qres.2001.2233

Augustinus, P., Fink, D., Fletcher, M., Thomas, I., 2017. Re-assessment of the mid to late Quaternary glacial and environmental history of the Boco Plain, western Tasmania. Quaternary Science Reviews, 160, 31. doi: 10.1016/j.quascirev.2017.01.015

790 Barrows,T.T., John O Stone, L.Keith Fifield, Richard G Cresswell, 2002. The timing of the Last Glacial
791 Maximum in Australia, Quaternary Science Reviews 21, 1–3, 159-173.

792 Barrows, T.T., Juggins, S., de Deckker, P., Calvo, E., Pelejero, C., 2007. Long-term sea surface
793 temperature and climate change in the Australian-New Zealand region: Australian-New Zealand
794 climate change. Paleoceanography 22 (2), PA2215.

795 Barton, C. E., and McElhinny, M.W., 1981. A 10,000 year geomagnetic secular variation record from
796 three Australian maars. Geophysical Journal of the Royal Astronomical Society 67, 465–485.

797 Beer, J., 2012. Cosmogenic Radionuclides: Theory and Applications in the Terrestrial and Space
798 Environments. Springer Berlin.

799 Blaauw, M., and Christen, J.A., 2011. Flexible paleoclimate age-depth models using an autoregressive
800 gamma process. Bayesian Analysis 6, 457-474

801 Blaauw, M., 2012. Out of tune: the dangers of aligning proxy archives. Quaternary Science Reviews
802 36, 38-49.

803 Bostock, H.C., T.T. Barrows, L. Carter, Z. Chase, G. Cortese, G.B. Dunbar, M. Ellwood, B. Hayward, W.
804 Howard, H.L. Neil, T.L. Noble, A. Mackintosh, P.T. Moss, A.D. Moy, D. White, M.J.M. Williams, L.K.
805 Armand, 2013. A review of the Australian–New Zealand sector of the Southern Ocean over the last
806 30 ka (Aus-INTIMATE project), Quaternary Science Reviews 74, 35-57,
807 https://doi.org/10.1016/j.quascirev.2012.07.018.

808 Bøtter-Jensen, L., Bulur, E., Duler, G. A. T., and Murray, A. S., 2000. Advances in luminescence
809 instrument systems. Radiation Measurements, 32, 523–528.

810 Bourlès, D.L., Raisbeck, G.M., Yiou, F., 1989. 10Be and 9Be in Marine sediments and their potential
811 for dating. Geochim. Cosmochim. Acta53 (2), 443–452.

812 Bradley, J., 1954. Geology of the West Coast Range of Tasmania. Papers and Proceedings of the
813 Royal Society of Tasmania, Vol. 88, p. 193–243.

814 Braucher, R., Guillou, V., Bourlès, D.L., Arnold, M., Aumaître, G., Keddadouche, K., Nottoli, E., 2015.
815 Preparation of ASTER in-house 10Be/9Be standard solutions. Nucl. Instrum. Methods Phys. Res.,
816 Sect. B, Beam Interact. Mater. Atoms361, 335–340.

817 Brennan, B. J. Beta doses to spherical grains. Radiat. Meas. 37, 299–303 (2003).

818 Briant, R., and Bateman, M.D., 2009. Luminescence dating indicates radiocarbon age
819 underestimation in late Pleistocene fluvial deposits from eastern England. Journal of Quaternary
820 Science. DOI: 10.1002/jqs.1258

821 Brown, M.C., F. Donadini, M. Korte, A. Nilsson, K. Korhonen, A. Lodge, S.N. Lengyel, C.G. Constable,
822 2015. GEOMAGIA50.v3: 1. General structure and modifications to the archeological and volcanic
823 database, Earth Planets Space 67:83, doi:10.1186/s40623-015-0232-0.

824 Channell, J.E.T., Singer, B.S., Jicha, B.R., 2020. Timing of Quaternary geomagnetic reversals and
825 excursions in volcanic and sedimentary archives, Quaternary Science Reviews 228,
826 106114,https://doi.org/10.1016/j.quascirev.2019.106114.

827 Channell, J.E.T., R.J. Harrison, I. Lascu, I.N. McCave, F.D. Hibbert, W.E.N. Austin, 2016. Magnetic
828 record of deglaciation using FORC-PCA, sortable-silt grain size, and magnetic excursion at 26 ka, from

the Rockall Trough (NE Atlantic), Geochem.Geophys. Geosyst. 17, 1823–1841, doi:10.1002/2016GC006300.

Chen, L., Heslop, D., Roberts, A. P., Chang, L., Zhao, X., McGregor, H. V., Marino, G., Rodriguez-Sanz, L., Rohling, E. J., & Pälike, H. (2017). Remanence acquisition efficiency in biogenic and detrital magnetite and recording of geomagnetic paleointensity. Geochemistry, Geophysics, Geosystems, 18, 1435– 1450. https://doi.org/10.1002/2016GC006753

Chmeleff, J., von Blanckenburg, F, Kossert, K., Jakob, D., 2010. Determination of the 10Be half-life by multicollector ICP-MS and liquid scintillation counting. Nucl. Instrum. Methods Phys. Res., Sect. B, Beam Interact. Mater. Atoms268 (2), 192–199.

Clarkson, C., Jacobs, Z., Marwick, B. et al. Human occupation of northern Australia by 65,000 years ago. Nature 547, 306–310 (2017). https://doi.org/10.1038/nature22968

Colhoun, E.A., Pola, J.S., Barton, C.E. and Heijnis, H. 1999. Late Pleistocene vegetation and climate history of Lake Selina, western Tasmania. Quaternary International 57/58:5-23.

Colman, S.M., Kaufman, D.S., Bright, J., Heil, C., King, J.W., Dean, W.E., Rosenbaum, J.G., Forester, R.M., Bischoff, J.L., Perkins, M., McGeehin, J.P., 2006. Age model for a continuous, ca 250-ka Quaternary lacustrine record from Bear Lake, Utah-Idaho. Quaternary Science Reviews 25, 2271-2282.

Constable, C.G., 1985. Eastern Australian geomagnetic field intensity over the past 14000 yr. Geophys. J. R. astr. Soc. 81, 121-130.

Constable, C.G., and M. W. McElhinny, 1985. Holocene geomagnetic secular variation records from north-eastern Australian lake sediments, Geophysical Journal International 81 (1), 103–120, https://doi.org/10.1111/j.1365-246X.1985.tb01353.x

Constable, C.G., Korte, M., Panovska, S., 2016. Persistent high paleosecular variation activity in southern hemisphere for at least 10 000 years, Earth and Planetary Science Letters 453, 78-86.

Cosgrove, R 1999. Forty-two degrees south: the archaeology of Late Pleistocene Tasmania, Journal of World Prehistory 13, 357-402.

Czymzik, M., Muscheler, R., Brauer, A., Adolphi, F., Ott, F., Kienel, U., et al., 2015. Solar cycles and depositional processes in annual Be-10 from two varved lake sediment records. Earth and Planetary Science Letters 428, 44–51. https://doi.org/10.1016/j.epsl.2015.07.037

Dankers, P., 1981. Relationship between median destructive field and remanent coercive forces for dispersed natural magnetite, titanomagnetite and hematite. Geophys. J. R. Astron. Soc. 64, 447–461.

de Abreu, L., Shackleton, N. J., Schönfeld, J., Hall, M., Chapman, M., 2003. Millennial-scale oceanic climate variability off the Western Iberian margin during the last two glacial periods, Marine Geology 196 (1–2), 1-20, https://doi.org/10.1016/S0025-3227(03)00046-X.

de Deckker, P, Arnold, L, van der Kaars, W et al., 2019, Marine Isotope Stage 4 in Australasia: A full glacial culminating 65,000 years ago - Global connections and implications for human dispersal, Quaternary Science Reviews 204, 187-207.

Du, Y. J., Zhou, W. J., Xian, F., Qiang, X. K., Kong, X. H., Zhao, G. Q., et al., 2018. 10Be signature of the Matuyama-Brunhes transition from the Heqing paleolake basin. Quaternary Science Reviews, 199(1), 41–48. https://doi.org/10.1016/j.quascirev.2018.09.020

869 Duller, G.A.T., 2003. Distinguishing quartz and feldspar in single grain luminescence measurements.
870 Radiation Measurements 37, 161–165.

871 Duller, G.A.T., 2004. Luminescence dating of Quaternary sediments: recent advances. Journal of
872 Quaternary Science 19, 183–192.

873 Egli, R., 2004. Characterization of individual rock magnetic components by analysis of remanence
874 curves, 1. Unmixing natural sediments. Stud Geophys Geod 48, 391–446

875 Egli, R., Chen, A. P., Winklhofer, M., Kodama, K. P., and Horng, C.-S. (2010), Detection of
876 noninteracting single domain particles using first-order reversal curve diagrams, Geochem. Geophys.
877 Geosyst., 11, Q01Z11, doi:10.1029/2009GC002916.Egli, R., 2013. VARIFORC: An optimized protocol
878 for calculating non-regular first-order reversal curve (FORC) diagrams. Global and Planetary Change,
879 110, 302–320. https://doi.org/10.1016/j.gloplacha.2013.08.003

880 Falster, G., Tyler, J., Grant, K., Tibby, J., Turney, C., Löhr, S., Jacobsen, G., Kershaw, A.P., 2018.
881 Millennial-scale variability in south-east Australian hydroclimate between 30,000 and 10,000 years
882 ago, Quaternary Science Reviews 192, 106-122. https://doi.org/10.1016/j.quascirev.2018.05.031.

883 Fitzsimmons, K.E., Stern, N., Murray-Wallace, C.V., Truscott, W., Pop, C., 2015. The Mungo Mega-
884 Lake Event, Semi-Arid Australia: Non-Linear Descent into the Last Ice Age, Implications for Human
885 Behaviour. PLOS ONE 10 (6), 0127008. https://doi.org/10.1371/journal.pone.0127008

886 Fletcher, M.-S., and Thomas, I., 2010. A Holocene record of sea level, vegetation, people and fire
887 from western Tasmania, Australia. The Holocene 20 (3), 351–361.
888 https://doi.org/10.1177/0959683609351903

889 Fletcher, M.-S., and Moreno, P.I., 2012. Have the Southern Westerlies changed in a zonally
890 symmetric manner over the last 14,000 years? A hemisphere-wide take on a controversial problem,
891 Quaternary International 253, 32-46, https://doi.org/10.1016/j.quaint.2011.04.042.

892 Francus, P., 2015. Standardization and Calibration of X-Radiographs Acquired with the ITRAX Core
893 Scanner. In book: (Eds Pierre Francus, Kinuyo Kanamaru, David Fortin) Micro-XRF Studies of
894 Sediment Cores. 10.1007/978-94-017-9849-5_20

895 France, D. E., and F. Oldfield (2000), Identifying goethite and hematite from rock magnetic
896 measurements of soils and sediments, J. Geophys. Res., 105, 2781– 2795.

897 Frank, M., Schwarz, B., Baumann, S., Kubik, P.K., Suter, M., Mangini, A., 1997. A 200 ka record of
898 cosmogenic radionuclide production rate and geomagnetic field intensity from 10Be in globally
899 stacked deep-sea sediments. Earth Planet. Sci. Lett. 149, 121-129.

900 Fritz, S., Baker, P., Lowenstein, T., Seltzer, G., Rigsby, C., Dwyer, G., Tapia, P.M., Arnold, K.K., Ku, T.-L.,
901 Luo, S., 2004. Hydrologic variation during the last 170,000 years in the southern hemisphere tropics
902 of South America. Quaternary Research, 61(1), 95-104. doi:10.1016/j.yqres.2003.08.007

903 Galbraith, R.F., Roberts, R.G., Laslett, G.M., Yoshida, H., Olley, J.M., 1999. Optical dating of single and
904 multiple grains of quartz from Jinmium rock shelter, northern Australia: Part I, experimental design
905 and statistical models. Archaeometry 41, 339–364.

906 Gale, S.J., Cook, D., Dorrington, N.J., 2013. The eastern Australian magnetic inclination record: Dating
907 the recent past and re-assessing the historical geomagnetic archive. The Holocene 23, 398-415.

908 Garreaud, R., 2007: Precipitation and Circulation Covariability in the Extratropics. J. Climate, 20,
909 4789–4797, https://doi.org/10.1175/JCLI4257.1

910 Guerin, G., Mercier, N., Adamiec, G. (2011) Dose-rate conversion factors: update. Ancient TL 29, 5-8.

911 Guyard H., St-Onge G., Chapron E., Anselmetti F.S., Francus P. (2007) The Ad 1881 Earthquake-
912 Triggered Slump And Late Holocene Flood-Induced Turbidites From Proglacial Lake Bramant,
913 Western French Alps. In: Lykousis V., Sakellariou D., Locat J. (eds) Submarine Mass Movements and
914 Their Consequences. Advances in Natural and Technological Hazards Research, vol 27. Springer,
915 Dordrecht

916 Harrison, R.J., and Feinberg, J.M., 2008. FORCinel: an improved algorithm for calculating first-order
917 reversal curve distributions using locally weighted regression smoothing. Geochem. Geophys.
918 Geosystems 9, Q05016. https://doi.org/10.1029/2008GC001987.

919 Harrison, R., Muraszko, J., Heslop, D., Lascu, I., Muxworthy, A., & Roberts, A., 2018. An Improved
920 Algorithm For Unmixing First-Order Reversal Curve Diagrams Using Principal Component Analysis.
921 Geochemistry, Geophysics, Geosystems, 19 (5), 1595-1610. https://doi.org/10.1029/2018GC007511

922 Hendon, H.H., Thompson, D.W.J., Wheeler, M.C., 2007. Australian rainfall and surface temperature
923 variations associated with the Southern Hemisphere annular mode. Journal of Climate 20 (11), 2452-
924 2467.

925 Henry, B. (2007). Magnetic Mineralogy, Changes due to Heating. In D. Gubbins & E. Herrero-Bervera
926 (Eds.), Encyclopedia of Geomagnetism and Paleomagnetism (pp. 512–515). Springer Netherlands.
927 https://doi.org/10.1007/978-1-4020-4423-6_179Heslop, D., Roberts, A., Chang, L., 2014.
928 Characterizing magnetofossils from first-order reversal curve (FORC) central ridge signatures.
929 Geochemistry, Geophysics, Geosystems. 15. 10.1002/2014GC005291.

930 Hogg, A., Heaton, T., Hua, Q., Palmer, J., Turney, C., Southon, J., Bayliss, A., Blackwell, P., Boswijk, G.,
931 Bronk Ramsey, C., Petchey, F., Reimer, P., Reimer, R., & Wacker, L. (2020). SHCal20 Southern
932 Hemisphere calibration, 0–55,000 years cal BP. Radiocarbon, 62.

933 Horiuchi, K., E.L. Goldberg, K. Kobayashi, T. Oda, T. Nakamura, T. Kawai, 2001. Climate-induced
934 variations of cosmogenic beryllium-10 in the sediments of Lake Baikal of the last 150ky from AMS,
935 SRXRF and NAA data. Nuclear Instruments and Methods in Physics Research Section A: Accelerators,
936 Spectrometers, Detectors and Associated Equipment 470, 1–2, 396-404,
937 https://doi.org/10.1016/S0168-9002(01)01085-3.

938 Horiuchi, K., K. Kamata, S. Maejima, S. Sasaki, N. Sasaki, T. Yamazaki, S. Fujita, H. Motoyama, H.
939 Matsuzaki, 2016. Multiple 10Be records revealing the history of cosmic-ray variations across the
940 Iceland Basin excursion. Earth Planet. Sci. Lett. 440, 105-114.

941 Howard, K., and Haines, P., 2007. The geology of Darwin Crater, western Tasmania, Australia. Earth
942 and Planetary Science Letters 260, 328-339. 10.1016/j.epsl.2007.06.007.

943 Huntley, D.J., Godfreysmith, D.I., Thewalt, M.L.W., 1985. Optical dating of sediments. Nature 313,
944 105–107.

945 Ingham, E., Turner, G. M., Conway, C. E., Heslop, D., Roberts, A. P., Leonard, G., Townsend, D., &
946 Calvert, A. (2017). Volcanic records of the Laschamp geomagnetic excursion from Mt Ruapehu, New
947 Zealand. Earth and Planetary Science Letters, 472, 131–141.
948 https://doi.org/10.1016/j.epsl.2017.05.023

Jacobs, Z. & Roberts, R. G. (2015). An improved single grain OSL chronology for the sedimentary deposits from Diepkloof Rockshelter, Western Cape, South Africa. J. Archaeol. Sci. 63, 175–192

Jouzel, J., V. Masson-Delmotte, O. Cattani, G. Dreyfus, S. Falourd, G. Hoffmann, B. Minster, J. Nouet, J. M. Barnola, J. Chappellaz, H. Fischer, J. C. Gallet, S. Johnsen, M. Leuenberger, L. Loulergue, D. Luethi, H. Oerter, F. Parrenin, G. Raisbeck, D. Raynaud, A. Schilt, J. Schwander, E. Selmo, R. Souchez, R. Spahni, B. Stauffer, J. P. Steffensen, B. Stenni, T. F. Stocker, J. L. Tison, M. Werner, E. W. Wolff, 2007. Orbital and Millennial Antarctic Climate Variability over the Past 800,000 Years. Science 10 Aug 2007: 793-796.

Kemp, C., Tibby, J., Arnold, L., Barr, C., 2019. Australian hydroclimate during Marine Isotope Stage 3: A synthesis and review. Quaternary Science Reviews 204. 10.1016/j.quascirev.2018.11.016.

Kiernan, K., Jones, R. and Ranson, D. 1983. New evidence from Fraser Cave for glacial age man in Southwest Tasmania. Nature 301:28-32

King, J.W., Banerjee, S.K., Marvin, J., 1983. A new rock-magnetic approach to selecting sediments for geomagnetic paleointensity studies: application to paleointensity for the last 4000 years. J. Geophys. Res. 88, 5911-5921.

Kirschvink, J.L., 1980. The least-squares line and plane and the analysis of paleomagnetic data. Geophys. J. Roy. Astr. Soc. 62, 699-718.

Korschinek, G., Bergmaier, A., Faestermann, T., Gerstmann, U.C., Knie, K., Rugel, G., Wallner, A., Dillmann, I., Dollinger, G., Lierse von Gostomski, Ch., Kossert, K., Maiti, M., Poutivtsev, M., Remmert, A., 2010. A new value for the half-life of 10Be by heavy-ion elastic recoil detection and liquid scintillation counting. Nucl. Instrum. Methods Phys. Res. B268 (2), 187–191.

Korte, M., Maxwell C. Brown, Sydney R. Gunnarson, Andreas Nilsson, Sanja Panovska, Ingo Wardinski, Catherine G. Constable, 2019. Refining Holocene geochronologies using palaeomagnetic records, Quaternary Geochronology 50, 47-74. https://doi.org/10.1016/j.quageo.2018.11.004.

Lagroix, F., & Guyodo, Y. (2017). A New Tool for Separating the Magnetic Mineralogy of Complex Mineral Assemblages from Low Temperature Magnetic Behavior. Frontiers in Earth Science, 5, 61.

Laj, C., and Channell, J. E. T., 2015. “Geomagnetic excursions,” Treatise in Geophysics, 2nd Edition, Vol. 5: Geomagnetism, eds G. Schubert and M. Kono (Amsterdam: Elsevier), 343–386.

Laj, C., Kissel, C., Beer, J., 2004. High Resolution Global Paleointensity Stack since 75 kas (GLOPIS-75) calibrated to absolute values, in Timescales of the Geomagnetic Field, eds J. E. T. Channell, D. V. K. Kent, W. Lowrie, and J. G. Meert (AGU Monogr. Ser. vol. 145) (Washington, DC: American Geophysical Union), 255–265. doi: 10.1029/145gm19

Lal, D. and Peters, B., 1967. Cosmic rays produced radioactivity on the Earth. Cosmic Rays II, Handbuch der Physik / Encyclopedia of Physick, Vol. 46, No. 2, pp. 551-612 Berlin, Springer-Verlag

Lambert, F., Bigler, M., Steffensen, J. P., Hutterli, M., and Fischer, H., 2012. Centennial mineral dust variability in high-resolution ice core data from Dome C, Antarctica, Clim. Past 8, 609–623, https://doi.org/10.5194/cp-8-609-2012

Liddicoat, J. C., and Coe, R. S., 1979. Mono Lake geomagnetic excursion, J. Geophys. Res. 84 (B1), 261– 271, doi:10.1029/JB084iB01p00261.

Lisé-Pronovost, A, G. St-Onge, C. Gogorza, G. Jouve, P. Francus, B. Zolitschka, 2014. Rock-magnetic signature of precipitation and extreme runoff events in south-eastern Patagonia since 51,200 cal BP from the sediments of Laguna Potrok Aike, Quaternary Science Reviews 98, 110-125, https://doi.org/10.1016/j.quascirev.2014.05.029.

Lisé-Pronovost, A., Fletcher, M.S., Mallett, T., Mariani, M., Lewis, R., Gadd, P., Herries, A., Blaauw, M., Heijnis, H., Hodgson, D., Pedro, J., 2019a. Scientific Drilling of Lake Sediments at Darwin Crater, Tasmania. Scientific Drilling 25, 1-14. https://doi.org/10.5194/sd-25-1-2019

Lisé-Pronovost, A., F. Salomon, J.-P. Goiran, G. St-Onge, A.I.R. Herries, J.-C. Montero-Serrano, D. Heslop, A.P. Roberts, V. Levchenko, A. Zawadzki, H. Heijnis, 2019b. Dredging and canal gate technologies in Portus, the ancient harbour of Rome, reconstructed from event stratigraphy and multi-proxy sediment analysis. Quaternary International 511, 78-93.

Lisiecki, L. E., and Lisiecki, P. A., 2002. Application of dynamic programming to the correlation of paleoclimate records, Paleoceanography, 17(D4), 1049, doi:10.1029/2001PA000733.

Lisiecki, L. E., and M. E. Raymo, 2005. A Pliocene-Pleistocene stack of 57 globally distributed benthic d18O records, Paleoceanography 20, PA1003, doi:10.1029/2004PA001071.

Liu, Q., Roberts, A.P., Larrasoana, J.C., Banerjee, S.K., Guyodo, Y., Tauxe, L. and Oldfield, F., 2012. Environmental magnetism: principles and applications. Reviews of Geophysics, 50(4).

Lund, S., L. Benson, R. Negrini, J. Liddicoat, S. Mensing, 2017. A full-vector paleomagnetic secular variation record (PSV) from Pyramid Lake (Nevada) from 47–17 ka: Evidence for the successive Mono Lake and Laschamp Excursions, Earth and Planetary Science Letters 458, 120-129, https://doi.org/10.1016/j.epsl.2016.09.036.

Lurcock, P. C. and G. S. Wilson, 2012. PuffinPlot: A versatile, user-friendly program for paleomagnetic analysis, Geochemistry, Geophysics, Geosystems, 13, Q06Z45, doi:10.1029/2012GC004098

Long, H. and Shen, J., 2014. Underestimated 14C-based chronology of late Pleistocene high lake-level events over the Tibetan Plateau and adjacent areas: Evidence from the Qaidam Basin and Tengger Desert. Science China: Earth Sciences, doi: 10.1007/s11430-014-4993-2.

Mackintosh, A. N., Barrows, T. T., Colhoun, E. A. and Fifield, L. K. 2006. Exposure dating and glacial reconstruction at Mt. Field, Tasmania, Australia, identifies MIS 3 and MIS 2 glacial advances and climatic variability. J. Quaternary Sci. 21, 363–376. ISSN 0267-8179

Maxbauer, D.P., Feinberg, J.M., Fox, D.L., 2016. MAX UnMix: A web application for unmixing magnetic coercivity distributions. Computers & Geosciences 95, 140-145.

Muscheler, R., Jürg Beer, Peter W. Kubik, H.-A. Synal, 2005. Geomagnetic field intensity during the last 60,000 years based on 10Be and 36Cl from the Summit ice cores and 14C, Quaternary Science Reviews 24, 16–17, 1849-1860, https://doi.org/10.1016/j.quascirev.2005.01.012.

Nathan, R.P., Mauz, B., 2008. On the dose-rate estimate of carbonate-rich sediments for trapped charge dating. Radiation Measurements 43, 14–25.

Nesje, A., 1992. A Piston Corer for Lacustrine and Marine Sediments. Arct. Alp. Res. 24, 603 257–259.https://doi.org/10.1080/00040851.1992.12002956

Nilsson, A., Muscheler, R, Snowball, I, Aldahan, A, Possnert, G, Augustinus, P, Atkin, D., Stephens, T., 2011, Multi-proxy identification of the Laschamp geomagnetic field excursion in Lake Pupuke, New

1028 Zealand, Earth and Planetary Science Letters 311, 1-2, 155-164.
1029 https://doi.org/10.1016/j.epsl.2011.08.050

1030 Nilsson, A., Suttie Neil, Hill Mimi J., 2018. Short-Term Magnetic Field Variations From the Post-
1031 depositional Remanence of Lake Sediments. Frontiers in Earth Science 6, 1-39.
1032 DOI=10.3389/feart.2018.00039

1033 O'Connell, C.S., Ruan, L. & Silver, W.L, 2018. Drought drives rapid shifts in tropical rainforest soil
1034 biogeochemistry and greenhouse gas emissions. Nat Commun 9, 1348.
1035 https://doi.org/10.1038/s41467-018-03352-3

1036 Pahnke, K., 2003. 340,000-Year centennial-scale marine record of Southern Hemisphere climatic
1037 oscillation. Science 301, 948-952.

1038 Panovska, S., M. Korte, C. C. Finlay, C. G. Constable, 2015. Limitations in paleomagnetic data and
1039 modelling techniques and their impact on Holocene geomagnetic field models, Geophysical Journal
1040 International 202, Issue 1, 402–418, https://doi.org/10.1093/gji/ggv137

1041 Panovska, S., Constable, C. G., Korte, M., 2018. Extending global continuous geomagnetic field
1042 reconstructions on timescales beyond human civilization. Geochem. Geophys. Geosys. 19, 4757–
1043 4772. doi: 10.1029/2018GC007966

1044 Peters, C. and Thompson, R., 1998. Magnetic Identification of Selected Natural Iron Oxides and
1045 Sulphides, Journal of Magnetism and Magnetic Materials, Vol. 183, No. 4, 365-374.
1046 doi:10.1016/S0304-8853(97)01097-4

1047 Peters, C., and M. J. Dekkers, 2003. Selected room temperature magnetic parameters as a function
1048 of mineralogy, concentration and grain size, Phys. Chem. Earth 28, 659-667, doi:10.1016/S1474-
1049 7065(03)00120-7.

1050 Petherick, L., Bostock, H., Cohen, T. J., Fitzsimmons, K., Tibby, J., Fletcher, M. -S., Moss, P., Reeves, J.,
1051 Mooney, S., Barrows, T., Kemp, J., Jansen, J., Nanson, G. & Dosseto, A. (2013). Climatic records over
1052 the past 30 ka from temperate Australia - a synthesis from the Oz-INTIMATE workgroup. Quaternary
1053 Science Reviews 74 58-77.

1054 Pigati, J.S., et al. 2007. Development of low-background vacuum extraction and graphitization
1055 systems for 14C dating of old (40-60 ka) samples. Quaternary International 166, 4-14.

1056 Prescott, J.R., Hutton, J.T., 1994. Cosmic-ray contributions to dose rates for luminescence and ESR
1057 dating: large depths and long-term time variations. Radiation Measurements 23, 497–500.

1058 Pugh, R., Mccave, I., Hillenbrand, Claus-Dieter, Kuhn, Gerhard, 2009. Circum-Antarctic age modelling
1059 of Quaternary marine cores under the Antarctic Circumpolar Current: Ice-core dust–magnetic
1060 correlation. Earth and Planetary Science Letters 284, 113-123. 10.1016/j.epsl.2009.04.016.

1061 Roberts, A.P., 2008. Geomagnetic excursions: Knowns and unknowns, Geophys. Res. Lett., 35,
1062 L17307, doi:10.1029/2008GL034719.

1063 Roberts, A.P., and Winklhofer, M., 2004. Why are geomagnetic excursions not always recorded in
1064 sediments? Constraints from post-depositional remanent magnetization lock-in modelling. Earth
1065 Planet. Sci. Lett. 227, 345–359. doi: 10.1016/j.epsl.2004.07.040

1066 Roberts, A.P., Chang, L., Rowan, C. J., Horng, C.-S., and Florindo, F., 2011. Magnetic properties of
1067 sedimentary greigite (Fe3S4): An update, Rev. Geophys. 49, RG1002, doi:10.1029/2010RG000336

1068 Roberts, A.P., L. Tauxe, D. Heslop, 2013. Magnetic paleointensity stratigraphy and high-resolution
1069 Quaternary geochronology: successes and future challenges. Quat. Sci. Rev. 61, 1-16

1070 Roberts, R.G., Jacobs, Z., Li, B., Jankowski, N.R., Cunningham, A.C., Rosenfeld, A.B., 2015. Optical
1071 dating in archaeology: thirty years in retrospect and grand challenges for the future. Journal of
1072 Archaeological Science 56, 41–60.

1073 Roberts, R.G., Flannery, T.F., Ayliffe, L.K., Yoshida, H., Olley, J.M., Prideaux, G.J., Laslett, G.M.,
1074 Baynes, A., Smith, M.A., Jones, R., Smith, B.L., 2001. New Ages for the Last Australian Megafauna:
1075 Continent-Wide Extinction About 46,000 Years Ago, Science 292, 5523, 1888-1892.
1076 10.1126/science.1060264

1077 Rohling E.J., et al. 2017. Differences between the last two glacial maxima and implications for ice-
1078 sheet, δ18O, and sea-level reconstructions. Quat. Sci. Rev. 2017;176:1–28. doi:
1079 10.1016/j.quascirev.2017.09.009.

1080 Roucoux, K. H., Tzedakis, P. C., Lawson, I. T., & Margari, V., 2011. Vegetation history of the
1081 penultimate glacial period (Marine Isotope Stage 6) at Ioannina, north-west Greece. Journal of
1082 Quaternary Science 26, 616–626.https://doi.org/10.1002/jqs.1483

1083 Ruddiman, W. F., 2006. Orbital changes and climate, Quaternary Science Reviews 25 (23–24), 3092-
1084 3112, https://doi.org/10.1016/j.quascirev.2006.09.001

1085 Rule, S., B. W. Brook, S. G. Haberle, C. S. M. Turney, A. P. Kershaw, C. N. Johnson, 2012. The
1086 aftermath of megafaunal extinction: Ecosystem transformation in Pleistocene Australia. Science 335,
1087 1483–1486.

1088 Saltré, F., Chadoeuf, J., Peters, K.J. et al. 2019. Climate-human interaction associated with southeast
1089 Australian megafauna extinction patterns. Nat Commun 10, 5311 doi:10.1038/s41467-019-13277-0

1090 Shanahan, T.M., J.A. Peck, N. McKay, C.W. Heil, J. King, S.L. Forman, D.L. Hoffmann, D.A. Richards,
1091 J.T. Overpeck, C.A. Scholz, 2012. Age models for long lacustrine sediment records using multiple
1092 dating approaches – an example from Lake Bosumtwi, Ghana. Quat. Geochronol., 15, 47-60.

1093 Simon, Q., Ledru, M.-P., Sawakuchi, A. O., Favier, C., Mineli, T. D., Grohmann, C. H., Guedes, M.,
1094 Bard, E., Thouveny, N., Garcia, M., Tachikawa, K., & Rodríguez-Zorro, P. A ., 2020a .
1095 Chronostratigraphy of a 1.5±0.1 Ma composite sedimentary record from Colônia basin (SE Brazil):
1096 Bayesian modeling based on paleomagnetic, authigenic 10Be/9Be, radiocarbon and luminescence
1097 dating. Quaternary Geochronology, 58, 101081.
1098 https://doi.org/https://doi.org/10.1016/j.quageo.2020.101081

1099 Simon, Q., Thouveny, N., Bourlès, D.L., Valet, J-P., Bassinot, F., 2020b. Cosmogenic 10Be production
1100 records reveal dynamics of geomagnetic dipole moment (GDM) over the Laschamp excursion (20–60
1101 ka). Earth Planet. Sci. Lett. 550, 116547.

1102 Simon, Q., Suganuma, Y., Okada, M., Haneda, Y., ASTER Team, 2019. High-resolution 10Be and
1103 paleomagnetic recording of the last polarity reversal in the Chiba composite section: Dynamics of
1104 the Matuyama-Brunhes transition. Earth Planet. Sci. Lett. 519, 92-100.

1105 Simon, Q., Bourlès, D.L., Thouveny, N., Horng, J., Valet, J-P., Bassinot, F., Choy, S., 2018 .
1106 Cosmogenic signature of geomagnetic reversals and excursions from the Réuion event to the
1107 Matuyama-Brunhes transition (0.7 - 2.14 Ma interval). Earth Planet. Sci. Lett. 482, 510-524.

Simon, Q., Thouveny, N., Bourlès, D.L., Bassinot, F., Valet, J -P., Ménabréaz, L., Guillou, V., Choy, S., Beaufort, L., 2016a. Authigenic 10Be/9Be ratio signatures of the cosmogenic nuclide production linked to geomagnetic dipole moment variation since the Brunhes/Matuyama boundary, J. Geophys. Res. Solid Earth 121, 10.1002/2016JB013335.

Simon, Q., Thouveny, N., Bourlès, D.L., Nuttin, L., St-Onge, G., Hillaire-Marcel, C., 2016b. Authigenic 10Be/9Be ratios and 10Be-fluxes (230Thxs-normalized) in central Baffin Bay during the last glacial cycle: Paleoenvironmental implications. Quat. Sci. Rev. 140, 142-162.

Sniderman, J. M. K., Hellstrom, J., Woodhead, J. D., Drysdale, R. N., Bajo, P., Archer, M., Hatcher, L., 2019. Vegetation and climate change in southwestern Australia during the Last Glacial Maximum. Geophysical Research Letters 46, 1709–1720. https://doi.org/10.1029/2018GL080832

St-Onge, G., Mulder, T., Piper, D.J.W., Hillaire-Marcel, C. & Stoner, J.S., 2004. Earthquake and flood induced turbidites on the Saguenay Fjord (Québec): a Holocene paleoseismicity record. Quaternary Science Reviews, 23, 283-294.

Suganuma, Y., Y. Yokoyama, T. Yamazaki, K. Kawamura, C.-S. Horng, H. Matsuzaki, 2010. 10Be evidence for delayed acquisition of remanent magnetization in marine sediments: implication for a new age for the Matuyama–Brunhes boundary. Earth Planet. Sci. Lett., 296. 443-450,10.1016/j.epsl.2010.05.031

Suganuma, Y., Okuno, J., Heslop, D., Roberts, A.P., Yamazaki, T., Yokoyama, Y., 2011. Post-depositional remanent magnetization lock-in for marine sediments deduced from 10Be and paleomagnetic records through the Matuyama-Brunhes boundary. Earth Planet. Sci. Lett. 311, 39-52.

Tang, L., Zhou, W., Wang, X., Xian, F., Du, Y., Zhou, J., et al., 2019. Multidecadal- to centennial-scale 10Be variations in Holocene sediments of Huguangyan Maar Lake, South China. Geophysical Research Letters 46, 7634– 7642. https://doi.org/10.1029/2019GL082863

Valet, J -P, F. Bassinot, A. Bouilloux, D.L. Bourlès, S. Nomade, V. Guillou, F. Lopes, N. Thouveny, F. Dewilde, 2014. Geomagnetic, cosmogenic and climatic changes across the last geomagnetic reversal from Equatorial Indian Ocean sediments. Earth Planet. Sci. Lett., 397, 67-79.

Valet, J-P., Bassinot, F., Simon, Q., Savranskaia, T., Thouveny, N., Bourlès, D.L., 2019. Constraining the age of the last geomagnetic reversal from geochemical and magnetic analyses of Atlantic, Indian, and Pacific Ocean sediments. Earth Planet. Sci. Lett. 506, 323-331.

Van der Kaars, S., Miller, G., Turney, C., Cook, E., Nuernberg, D., Schönfeld, J., Kershaw, P., Lehman, S., 2017. Humans rather than climate the primary cause of Pleistocene megafaunal extinction in Australia. Nature Communications 8. 14142. 10.1038/ncomms14142.

Veres, D., Bazin, L., Landais, A., Toye Mahamadou Kele,H., Lemieux-Dudon, B., Parrenin, F., Martinerie, P., Blayo, E., Blunier, T., Capron, E., Chappellaz, J., Rasmussen, S., Severi, M., Svensson, A., Vinther, B., and Wolff, E., 2013. The Antarctic ice core chronology (AICC2012): an optimized multi-parameter and multi-site dating approach for the last 120 thousand years, Climate of the Past 9, 1733-1748, doi:10.5194/cp-9-1733-2013

Willenbring, J.K., von Blanckenburg, F., 2010. Meteoric cosmogenic beryllium-10 adsorbed to river sediment and soil: applications for Earth-surface dynamics. Earth-Sci. Rev. 98, 105–122.

1147 Williams, M., Cook, E., van der Kaars, S., Barrows, T., Shulmeister, J., Kershaw, P., 2009. Glacial and
1148 deglacial climatic patterns in Australia and surrounding regions from 35 000 to 10 000 years ago
1149 reconstructed from terrestrial and nearshore proxy data. Quat. Sci. Rev. 28, 2398-2419.

1150 Wintle, A.G., 2014. Luminescence dating methods. In: Holland, H.D., Turekian, K.K. (Eds), Treatise on
1151 Geochemistry (second edition), vol. 14, pp. 17–35. Elsevier, Oxford.

1152 Wintle A.G., 1997. Luminescence dating: laboratory procedures and protocols. Radiation
1153 Measurements 27, 769-817.

1154 Wintle, A.G. and Murray, A., 2006. A review of optically stimulated luminescence characteristic and
1155 their relevance in single-aliquot regeneration dating protocols. Radiation Measurements 41. 369-
1156 391. 10.1016/j.radmeas.2005.11.001.

1157 Woodward, C.A. and Gadd, P.S. 2018. The potential power and pitfalls of using the X-ray
1158 fluorescence molybdenum incoherent: Coherent scattering ratio as a proxy for sediment organic
1159 content, Quaternary International 514, 30-43.10.1016/j.quaint.2018.11.031

1160 Wroe, S. and Field, J., 2006. A review of the evidence for a human role in the extinction of Australian
1161 Megafauna and an alternative explanation. Quaternary Science Reviews 25. 2692-2703.

FIGURE CAPTIONS

Figure 1. Site location A) in the Southern Hemisphere mid-latitudes and B) in the West Coast Range of Tasmania where rainfall is strongly correlated to the westerly winds. A and B are modified from Lise-Pronovost et al (2019). C) Two sites were cored in the approximate center of Lake Selina. The 10 m contours and hydrographic data are from Land Information System Tasmania (LIST) and the satellite imagery from ESRI.

Figure 2. A) Cores LA, N1 and N2 simplified lithology, correlation and sampling. Note the different thickness of the Last Glacial Period sediment facies in cores N1 and N2. Individual core sections are indicated to the left of each lithology log. Core section N2-A was divided in sub-sections a and b after a sediment gap formed during splitting. Black zones indicate sampling locations for radiocarbon (^{14}C), magnetic analysis (mag), optically stimulated luminescence (OSL), and beryllium isotopes (Be). B) Large amplitude change in the XRF ratio Inc/coh is used to correlate the gravity core LA with the Nesje cores N1 and N2. C) The composite depth LAN2 is the reference depth scale used in this work. Data from core N1 is transferred to LAN2 depth using a series of 24 stratigraphic tie-points (they are the horizontal lines of the stratigraphic log) and linear interpolation.

Figure 3. Physical, elemental and magnetic properties of core TAS1402. Upper panel: XRF and beryllium data including pass-through radiation (RAD; density proxy), incoherence/coherence (Inc/coh; organic content proxy), authigenic ^{10}Be and ^{9}Be isotopes and elemental ratio Pb/Al (local runoff proxies), and Ti/K (detrital grain size proxy). Middle panel: magnetic properties including the remanence ratio kARM/IRM, median destructive field of the anhysteretic remanent magnetisation (MDF_{ARM}), and magnetisation ratio (Mr/Ms) (magnetic grain size proxies), S-ratio (proportion of low coercivity minerals), HIRM (content of high coercivity minerals). Lower panel: ferrimagnetic content proxies including the volumetric magnetic susceptibility (k_{LF}), natural remanent magnetisation (NRM) on log and linear scales, anhysteretic and isothermal remanent magnetizations (ARM and IRM). The simple lithology log with sediment facies is shown for the reference depth LAN2. The overlapping section N2-A for the magnetic grain size proxies is shown to illustrate finer particles are deposited at site N2 compared to site N1. Grey shading indicates facies IIa intervals with approximately one order of magnitude greater remanence acquisition efficiency.

Figure 4. Principal component analysis biplot of the micro-XRF core scanning data. The length and color of the arrow reflect the contribution per variable.

Figure 5. A) Measured moisture contents for OSL and DOS samples between 81 and 190 cm depth LAN2, where OSL ages were obtained. B) Gamma dose rates for the same OSL and DOS samples derived from ICP-MS(OES) measurements of U, Th and K and used for age determination. C) Beta dose rates for the same OSL and DOS samples obtained from GM-25-5 beta counting and used for age determination. D) The ratio of beta dose rates derived from GM-25-5 beta counting and ICP-MS(OES) measurements for the same OSL and DOS samples. The stippled line denotes unity. Error bars are all one standard error. The simple lithology log with sediment facies is shown.

Figure 6. A) Age-depth model from Bayesian modeling (rbacon; Blaauw and Christen, 2011) of calibrated radiocarbon (^{14}C) and optically stimulated luminescence (OSL) ages (Tables 1 and 2). The OSL ages are

obtained from core N1 and transferred to the reference depth LAN2 based on stratigraphic correlations (Supplementary Material 2). B) Contamination effect on radiocarbon ages (Pigati et al., 2007) explains the excluded "too young" ^{14}C ages that plateau at ca. 40 ka BP.

Figure 7. Magnetic mineralogy of Lake Selina interglacial sediments (facies I) and glacial sediment (facies II). Representative sample N1-A18 (81.8 cm depth LAN2) for facies I includes A) hysteresis loop, B) thermomagnetic curves of (top panel) magnetic remanence measured from room temperature to 10 Kelvin saturation isothermal remanent magnetisation (RTSIRM), and (base panel) magnetic susceptibility up to 700 °C, C) unmixed magnetic populations (P1, P2, P3) of the isothermal remanent magnetisation (IRM) acquisition curve (MaxUnmix; Maxbauer et al., 2016), and D) first order reversal curve (FORC) diagram (FORCinel; Harrison and Feinberg, 2008). Representative sample N1-C37 (365.3 cm depth LAN2) for facies II includes E) hysteresis loop, F) thermomagnetic curves, G) unmixed magnetic populations (MaxUnmix; Maxbauer et al., 2016), and H) FORC diagram (FORCinel; Harrison and Feinberg, 2008).

Figure 8. The biplot of the magnetic remanence ratios IRM(-300mT)/SIRM and ARM(40mT)/SARM informs on the mineralogy of the remanence carriers (Peters and Thompson, 1998). Greater ARM hardness (ARM(40mT)/SARM) in facies I also reflects finer magnetic grain size than in facies II (visible in Fig. 2).

Figure 9. Paleomagnetic directions results for A) raw data and B) data after selection criteria, and relative paleointensity estimates for C) raw data and D) selected data. A line is not used to connect the data points from duplicate core N2-A (blue) because of possibly disturbed stratigraphy. Grey shading indicates the non-selected intervals with approximately one order of magnitude greater remanence acquisition efficiency (cf. Figure 3). A few individual samples display peak values (out of scale) interpreted as having NRM overprint.

Figure 10. The paleomagnetic record from Lake Selina uppermost 2.25 m combines sediment magnetic remanence and authigenic beryllium isotopes. From left to right; the paleomagnetic inclination, relative declination and geomagnetic field intensity proxies (Be ratio and RPI). A line is not used to connect the data points from duplicate core N2-A (blue) because of possibly disturbed stratigraphy. The yellow rectangle at 100-117 cm depth LAN2 indicates excursional directions (duration about 10 kyr) and intensity (duration about 5 kry) at the time of the Laschamp geomagnetic excursion. The yellow rectangle at 91-95 cm depth LAN2 indicates a younger Be ratio maxima, however with inconclusive magnetic remanence results. The geomagnetic field intensity proxies are scaled and the Be ratio axis is reversed. The grey highlight indicates the best fit among geomagnetic field intensity proxies where lock-in depth in RPI appears to be absent.

Figure 11. Proxy data from Lake Selina (this study) and Antarctica EDC ice core (Jouzel et al, 2007; Lambert et al, 2012; Veres et al, 2013) used to build the Match-Climate age model using Match dynamic programing (Liesicki and Liesicki, 2002). A) Temperature proxies incoherence/coherence (inc/coh; this study) and dD (Jouzel et al, 2007), and B) atmospheric circulation proxies Pb/Al (this study) and dust flux (Lambert et al, 2012). The top two curves from Lake Selina are versus depth and Match-Climate age, and the lower curves are the reference proxy data from Antarctica on the Antarctic Ice Core Chronology 2012 (Veres et al, 2013). Vertical dashed lines indicate the six tie-points used for Match programming. Correlation coefficients are indicated for the Match-Climate dated interval 18-266 ka and for the highlighted interval in grey representing the period 20-60 ka (MIS2 and 3).

Figure 12. Lake Selina age-depth models. Age of selected stratigraphic changes are indicated on the right according to the age models Radiometric, Match-Climate and Match-Dipole, and compared to the MIS boundary ages (Liesicki and Raymo, 2005). The interpreted MIS for Lake Selina are indicated next to the simplified stratigraphic log.

Figure 13. Lake Selina geomagnetic field intensity proxies (Be ratio and RPI) on the age-depth models A) Radiometric, B) Match-Climate, and C) Match-Dipole, compared to D) dipole references (Be stack, Simon et al., 2016; GLOPIS, Laj et al, 2014; GGF100k, Panovska et al, 2018). The highlighted interval in grey represents the period 20-60 ka (MIS2 and 3) and the best fit interval between RPI and Be ratio defined in Fig. 10. Yellow shading indicates the geomagnetic intensity low associated to the Laschamp excursion (41 ka). The comparison illustrates the age overestimation of Match-Climate over the period 20-60 ka BP because of poor correlation in climate proxies (Fig. 9) and possibly disturbed stratigraphy of core N2-A. Note the different trends in dipole references for the period 60-80 ka BP.

Table 1. Radiocarbon ages from TAS1402. The selected samples for age-depth modelling are bold.

Lab ID	Core	Section depth (cm)	Depth LAN2 (cm)	+/- error depth	Radiocarbon age	error (1 sigma)	Min Calibrated age (cal BP)	Max Calibrated age (cal BP)	Mean Age (cal BP)
surface			**0.0**		**-64**				**-64**
D-AMS 009187	**LA**	**11-11.5**	**11.3**	**0.3**	**2614**	**27**	**2548**	**2756**	**2652**
D-AMS 012498	**LA**	**13.75-14**	**13.9**	**0.1**	**3649**	**28**	**3876**	**3978**	**3927**
D-AMS 017905	**LA**	**17.25-18**	**17.6**	**0.4**	**4589**	**26**	**5063**	**5317**	**5190**
D-AMS 017906	**LA**	**30.5-31**	**30.8**	**0.3**	**7194**	**33**	**7945**	**8010**	**7978**
D-AMS 009086	**LA**	**37-37.5**	**37.3**	**0.3**	**8515**	**39**	**9478**	**9531**	**9505**
D-AMS 014240	**LA**	**42.25-42.5**	**42.4**	**0.1**	**8723**	**36**	**9553**	**9672**	**9613**
D-AMS 014241	**LA**	**52.25-52.5**	**52.4**	**0.1**	**10414**	**35**	**12147**	**12462**	**12305**
D-AMS 014242	**LA**	**62.25-62.5**	**62.4**	**0.1**	**11726**	**41**	**13496**	**13594**	**13545**
D-AMS 014243	**LA**	**67.75-68**	**67.9**	**0.1**	**12123**	**40**	**13860**	**14060**	**13960**
D-AMS 014244	**LA**	**72.25-72.5**	**72.4**	**0.1**	**12457**	**53**	**14327**	**14834**	**14581**
D-AMS 015348	**N2-A**	**23-23.25**	**73.1**	**0.1**	**12965**	**44**	**15356**	**15556**	**15456**
D-AMS 015349	**N2-A**	**30-30.25**	**80.1**	**0.1**	**14736**	**50**	**17948**	**18144**	**18046**
D-AMS 015350	N2-A	34-34.25	84.1	0.1	22857	86	27135	27259	27197
D-AMS 009079	N2-A	37-37.5	87.3	0.3	19048	71	22909	23016	22963
D-AMS 027826	N2-A	38-38.25	88.1	0.1	25130	106	29158	29503	29331
D-AMS 027827	N2-A	46.5-46.75	96.6	0.1	16581	61	19893	20087	19990
D-AMS 027828	N2-A	56.75-57	106.9	0.1	18510	68	22333	22449	22391
D-AMS 027829	N2-A	62.5-62.75	112.6	0.1	32971	180	37067	37557	37312
D-AMS 009080	N2-A	64.75-65.25	115.0	0.3	32778	181	36881	37380	37131
D-AMS 027830	N2-A	70-70.25	120.1	0.1	37330	276	41859	42160	42010
D-AMS 027831	N2-A	77-77.25	127.1	0.1	NDFB				
D-AMS 015351	N2-A	84-84.25	134.1	0.1	34529	219	39396	39829	39613
D-AMS 009082	N2-A	94.25-94.5	144.4	0.1	37542	249	41985	42214	42100
D-AMS 015352	N2-A	102-102.25	152.1	0.1	35920	246	40794	41205	41000
D-AMS 009084	N2-A	110-110.5	160.3	0.3	14883	51	18146	18244	18195
D-AMS 015335	N2-A	118-118.25	168.1	0.1	NDFB				
D-AMS 009088	N2-B	12.5-13	183.8	0.3	33494	182	37750	38718	38234
D-AMS 015354	N2-B	24.5-24.75	195.6	0.1	NDFB				
D-AMS 015355	N2-B	48.25-48.5	219.4	0.1	NDFB				

Table 2. Dose rate data, equivalent dose (D_e) and overdispersion (OD) values, and ages from core TAS1402-N1. The samples core section depths were transferred to LAN2 equivalent depth (Sup. Mat. Table 1).

					Environmental dose rate (Gy/ka)								
Sample	**Core**	**Section depth (cm)**	**Average depth LAN2 (cm)**	**Water content (%)**	**Gamma**	**Beta**	**Cosmic**	**Alpha**	**Total**	**No of aliquots**	**CAM D_e (Gy)**	**Overdispersion (%)**	**OSL age (ka)**
OSL1	N1-A	44-49	83.5	40 (30)	0.75 ± 0.05	1.26 ± 0.07	0.13 ± 0.02	0.03	2.17 ± 0.09	6/6	55.7 ± 2.7	4.8 ± 7.6	25.7 ± 1.7
OSL2/3	N1-A	55-61	90.0	40 (32)	0.73 ± 0.03	1.15 ± 0.07	0.13 ± 0.02	0.03	2.04 ± 0.08	10/10	49.2 ± 1.9	0	24.2 ± 1.4
OSL4	N1-A	67-74	102.2	40 (22)	0.64 ± 0.04	0.99 ± 0.05	0.12 ± 0.02	0.03	1.78 ± 0.06	10/10	62.2 ± 2.8	14.5 ± 5.8	35 ± 2.1
OSL5	N1-A	74-80	111.2	40 (20)	0.64 ± 0.03	1.04 ± 0.05	0.12 ± 0.02	0.03	1.83 ± 0.06	9/10	75.6 ± 4.8	11.6 ± 6.9	41.3 ± 3.1
OSL6	N1-A	80-86	117.2	40 (25)	0.67 ± 0.04	1.05 ± 0.05	0.12 ± 0.02	0.03	1.87 ± 0.07	10/10	102.1 ± 11.5	32.2 ± 8.7	54.6 ± 6.6
OSL7	N1-A	89-92	123.5	40 (31)	0.67 ± 0.04	1.11 ± 0.07	0.12 ± 0.02	0.03	1.93 ± 0.08	9/10	113.6 ± 7.0	14.6 ± 5.4	58.9 ± 4.6
OSL8	N1-A	99-101	132.5	40 (32)	0.73 ± 0.05	1.12 ± 0.07	0.12 ± 0.02	0.03	2.01 ± 0.09	10/10	113.7 ± 8.0	18.8 ± 5.7	56.7 ± 4.8
OSL9	N1-A	105-108	137.3	40 (30)	0.71 ± 0.05	1.27 ± 0.07	0.12 ± 0.02	0.03	2.13 ± 0.09	9/10	144.7 ± 7.9	11.0 ± 5.3	67.9 ± 4.9
OSL10	N1-A	108-111	139.8	40 (29)	0.71 ± 0.05	1.12 ± 0.06	0.12 ± 0.02	0.03	1.99 ± 0.08	9/10	126.4 ± 7.5	15.6 ± 4.8	63.6 ± 4.8
OSL11	N1-B	0-5	158.1	40 (26)	0.68 ± 0.04	1.00 ± 0.05	0.12 ± 0.02	0.03	1.83 ± 0.07	10/10	138.9 ± 5.5	5.8 ± 5.6	75.8 ± 4.4
OSL12	N1-B	5-10	163.8	40 (25)	0.67 ± 0.04	0.99 ± 0.05	0.12 ± 0.02	0.03	1.81 ± 0.07	9/10	144.5 ± 16.5	30.0 ± 8.9	79.8 ± 9.7
OSL13	N1-B	18-23	175.0	40 (24)	0.64 ± 0.04	0.93 ± 0.05	0.12 ± 0.02	0.03	1.72 ± 0.06	9/10	143.9 ± 6.1	21.7 ± 6.3	83.6 ± 5

Table 3. Beryllium isotopes results. Replicate measurements are italic.

Sample	Core	Section depth (cm)	Depth LAN2 (cm)	Measured $^{10}Be/^{9}Be$ (10^{-11})	Authigenic decay corrected ^{10}Be (10^{8} at.g^{-1})	Authigenic ^{9}Be (10^{16} at.g^{-1})	Authigenic decay corrected $^{10}Be/^{9}Be$ (10^{-8})
1	N1-A	1.2	43.7	3.146 ± 0.046	8.382 ± 0.124	0.508 ± 0.014	16.513 ± 0.514
4	N1-A	8.4	50.6	3.366 ± 0.048	9.422 ± 0.136	0.630 ± 0.013	14.949 ± 0.375
6	N1-A	13.2	55.3	4.951 ± 0.087	13.121 ± 0.231	0.790 ± 0.006	16.603 ± 0.318
9	N1-A	20.4	62.2	7.052 ± 0.122	15.227 ± 0.264	0.833 ± 0.012	18.281 ± 0.407
12	N1-A	27.6	69.1	7.927 ± 0.130	26.103 ± 0.427	1.771 ± 0.021	14.738 ± 0.298
15	N1-A	34.8	76.1	16.770 ± 0.280	36.718 ± 0.614	2.173 ± 0.065	16.895 ± 0.576
18	N1-A	42	81.8	9.803 ± 0.168	19.496 ± 0.335	1.073 ± 0.021	18.173 ± 0.473
20	N1-A	46.8	83.3	4.504 ± 0.078	9.787 ± 0.169	0.484 ± 0.010	20.230 ± 0.549
22	N1-A	51.6	84.0	6.345 ± 0.105	14.398 ± 0.238	0.726 ± 0.004	19.838 ± 0.346
24	N1-A	56.4	87.4	7.110 ± 0.179	15.505 ± 0.389	0.758 ± 0.010	20.449 ± 0.578
25	N1-A	58.8	89.2	5.744 ± 0.073	13.883 ± 0.176	0.735 ± 0.021	18.887 ± 0.600
26	N1-A	61.2	91.0	6.761 ± 0.170	14.991 ± 0.376	0.632 ± 0.013	23.735 ± 0.760
27	N1-A	63.6	92.8	7.432 ± 0.092	20.083 ± 0.249	0.869 ± 0.024	23.118 ± 0.702
27	*N1-A*	*63.6*	*92.8*	*6.084 ± 0.076*	*21.142 ± 0.263*	*0.908 ± 0.026*	*23.292 ± 0.739*
28	N1-A	66	94.6	6.182 ± 0.157	12.316 ± 0.312	0.440 ± 0.012	28.004 ± 1.030
28	*N1-A*	*66*	*94.6*	*3.716 ± 0.047*	*12.041 ± 0.151*	*0.521 ± 0.013*	*23.126 ± 0.645*
29	N1-A	68.4	96.7	3.368 ± 0.050	7.741 ± 0.116	0.393 ± 0.010	19.684 ± 0.597
30	N1-A	70.8	*100.0*	1.499 ± 0.041	3.504 ± 0.097	0.158 ± 0.004	22.144 ± 0.871
31	N1-A	73.2	103.3	2.613 ± 0.039	5.794 ± 0.087	0.262 ± 0.008	22.090 ± 0.738
32	N1-A	75.6	106.7	2.494 ± 0.065	5.591 ± 0.146	0.257 ± 0.006	21.793 ± 0.742
33	N1-A	78	110.0	3.484 ± 0.089	7.672 ± 0.196	0.332 ± 0.009	23.084 ± 0.869
34b	N1-A	80.4	113.3	2.795 ± 0.071	5.996 ± 0.153	0.252 ± 0.002	23.760 ± 0.648
34a	N1-A	82.8	115.9	4.299 ± 0.109	9.739 ± 0.247	0.421 ± 0.007	23.121 ± 0.705
35	N1-A	85.2	117.4	3.487 ± 0.089	8.117 ± 0.207	0.347 ± 0.004	23.390 ± 0.667
36	N1-A	87.6	118.8	6.764 ± 0.171	15.075 ± 0.380	0.710 ± 0.013	21.226 ± 0.660
37	N1-A	90	121.1	3.572 ± 0.051	7.872 ± 0.113	0.411 ± 0.009	19.135 ± 0.498
38	N1-A	92.4	123.5	5.875 ± 0.148	13.196 ± 0.332	0.626 ± 0.007	21.087 ± 0.579

39	N1-A	94.8	125.9	13.422	±	0.178	29.021	±	0.385	1.481	±	0.043	19.601	±	0.629
40	N1-A	97.2	128.3	9.994	±	0.250	23.112	±	0.577	1.087	±	0.006	21.257	±	0.544
41	N1-A	99.6	130.7	6.179	±	0.078	15.911	±	0.200	0.817	±	0.017	19.479	±	0.478
42	N1-A	102	132.6	10.647	±	0.268	23.735	±	0.597	1.092	±	0.006	21.736	±	0.560
44	N1-A	106.8	135.9	7.579	±	0.190	16.865	±	0.423	0.761	±	0.008	22.160	±	0.599
46	N1-A	111.6	139.9	6.864	±	0.114	15.245	±	0.254	0.761	±	0.011	20.030	±	0.449
48	N1-A	116.4	143.5	6.020	±	0.099	13.467	±	0.221	0.694	±	0.012	19.419	±	0.469
50	N1-A	121.2	146.9	5.447	±	0.091	10.664	±	0.179	0.499	±	0.008	21.375	±	0.499
53	N1-A	128.4	151.9	5.124	±	0.091	11.807	±	0.209	0.528	±	0.014	22.370	±	0.704
1	N1-B	1.2	156.8	5.452	±	0.090	11.620	±	0.193	0.561	±	0.004	20.700	±	0.367
4	N1-B	8.4	164.9	2.020	±	0.035	4.663	±	0.080	0.221	±	0.005	21.108	±	0.632
7	N1-B	15.6	172.0	3.862	±	0.065	8.867	±	0.150	0.392	±	0.004	22.630	±	0.445
9	N1-B	20.4	175.0	1.265	±	0.021	3.099	±	0.051	0.135	±	0.004	23.007	±	0.749
12	N1-B	27.6	182.7	3.137	±	0.046	6.992	±	0.103	0.361	±	0.011	19.352	±	0.642
15	N1-B	34.8	189.4	3.298	±	0.047	7.783	±	0.111	0.390	±	0.005	19.940	±	0.368
18	N1-B	42	196.2	4.689	±	0.069	10.606	±	0.156	0.500	±	0.010	21.197	±	0.532
21	N1-B	49.2	202.9	2.719	±	0.041	6.123	±	0.091	0.279	±	0.006	21.972	±	0.571
24	N1-B	56.4	209.7	1.891	±	0.030	4.484	±	0.072	0.198	±	0.005	22.694	±	0.655
27	N1-B	63.6	217.6	2.246	±	0.038	5.231	±	0.088	0.226	±	0.005	23.136	±	0.630
29	N1-B	68.4	222.3	3.661	±	0.053	8.328	±	0.120	0.400	±	0.008	20.825	±	0.518

Table 4. Average estimated sedimentation rates for each age model. The assigned marine isotope stages (MIS) for Lake Selina are shown in Figure 11. In cases where an age model does not cover an entire MIS, the covered sub-stages are indicted in parentheses.

	Average sedimentation rate (cm/ka)		
	Radiometric	Match-Climate	Match-Dipole
Facies			
I	5.1	5.2	1.6
II	1.5	2.6	1.5
MIS			
MIS 1	5.3		
MIS 2, 3, 4	1.5	2.5	1.5
MIS 5	1.9 (MIS 5a)	6.2	1.6 (MIS 5a, 5c)
MIS 6		2.4	
MIS 7		3.0	
MIS 8		1.9	

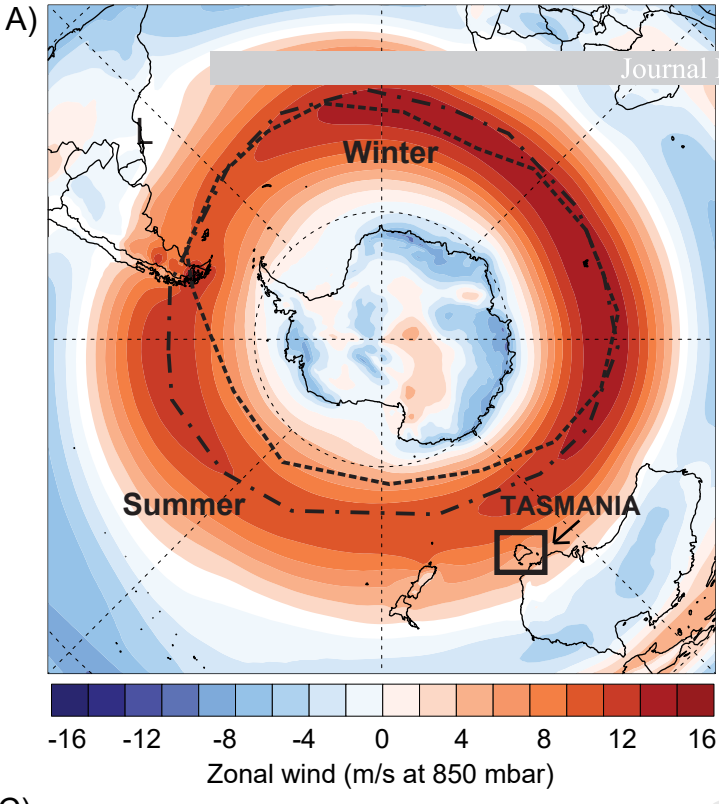

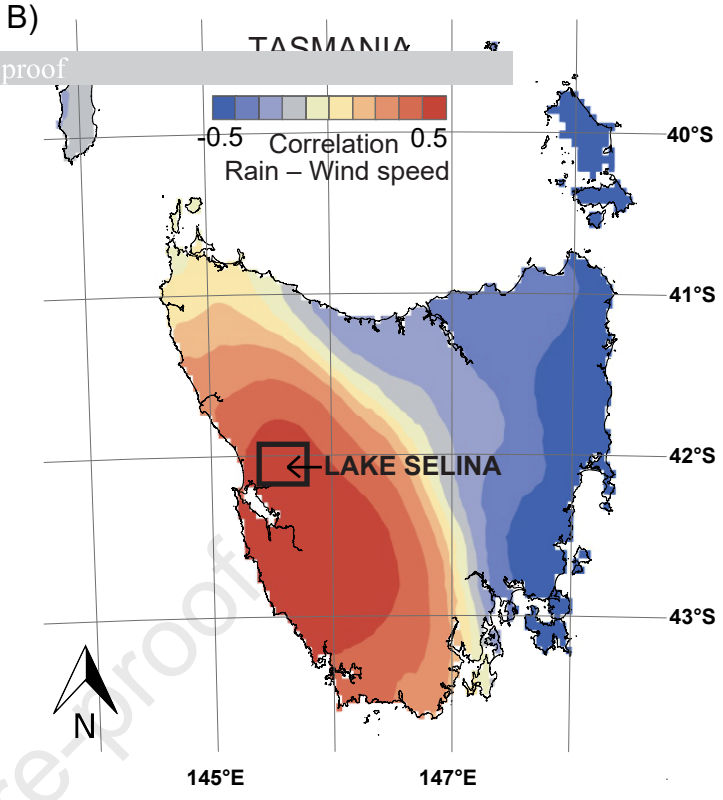

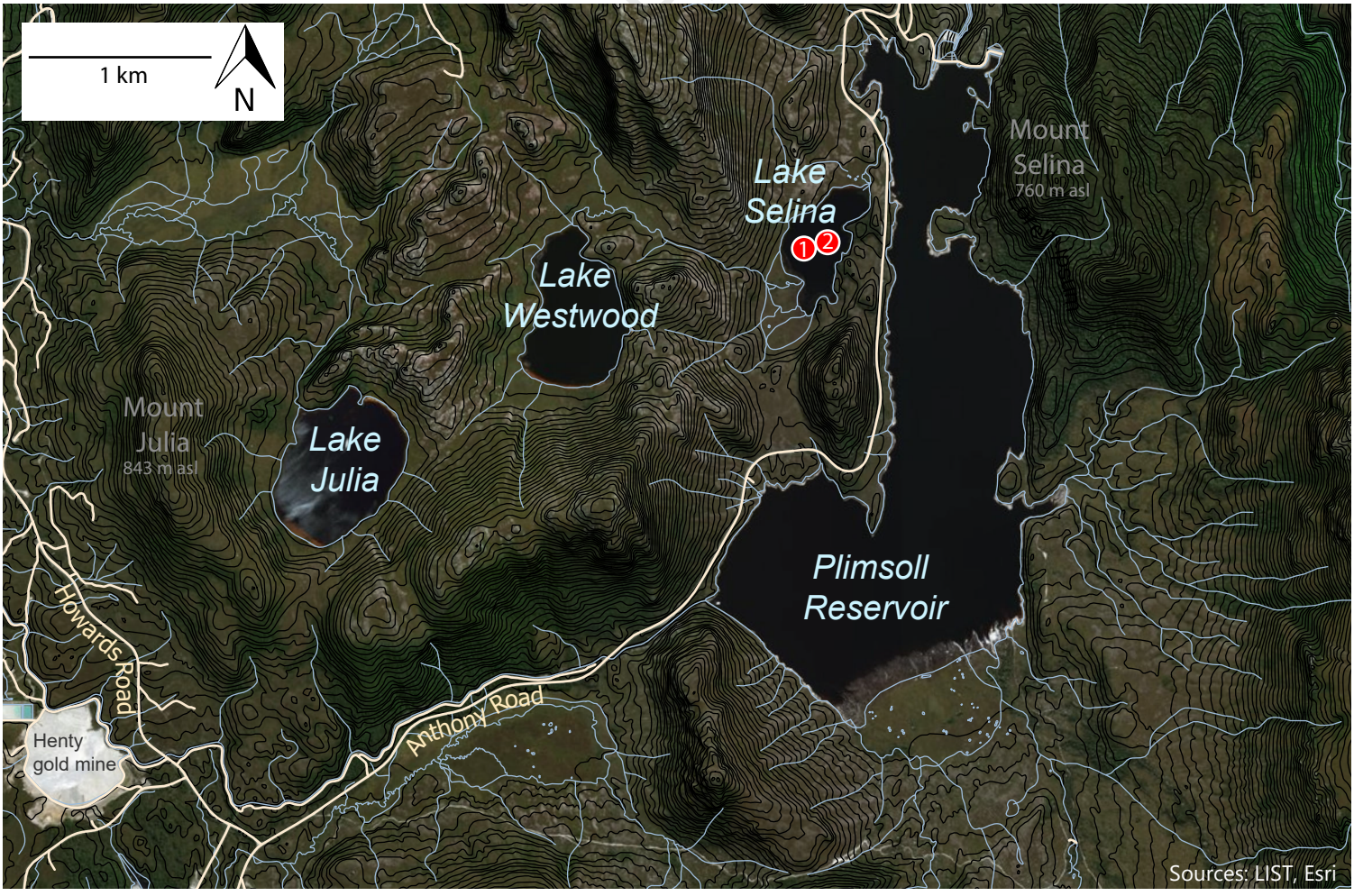

A) Cores correlation and sampling

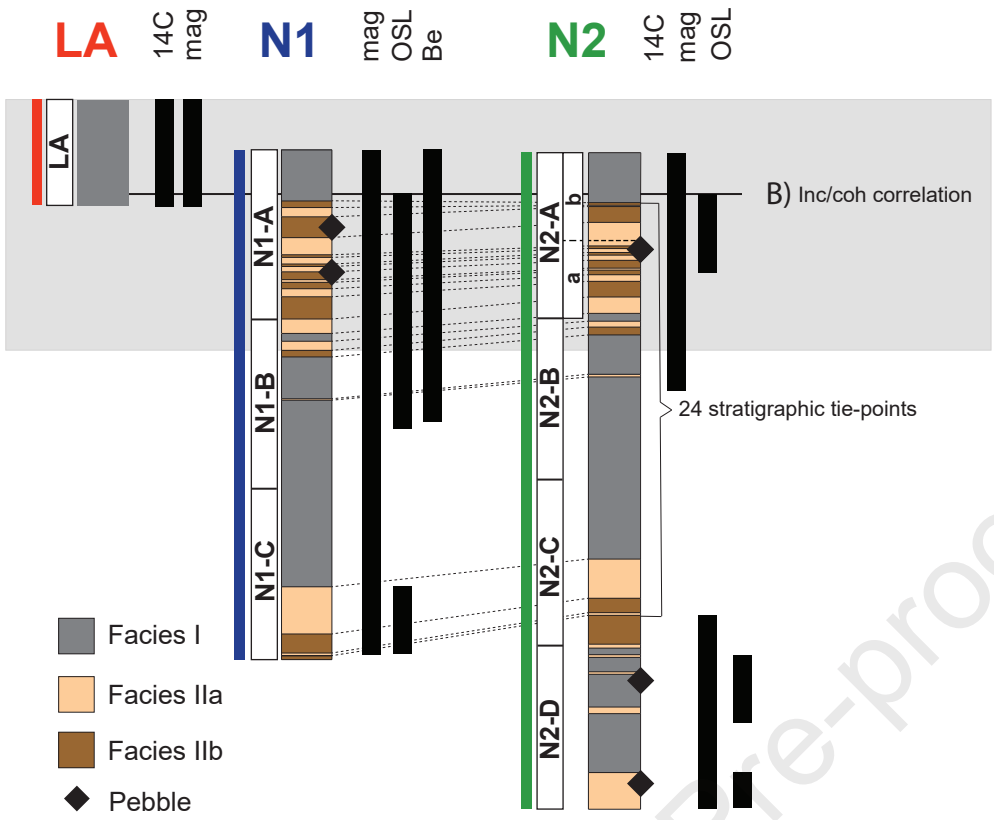

C) Reference depth scale

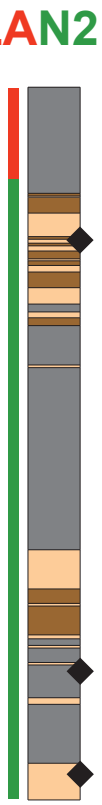

B) Inc/coh correlation

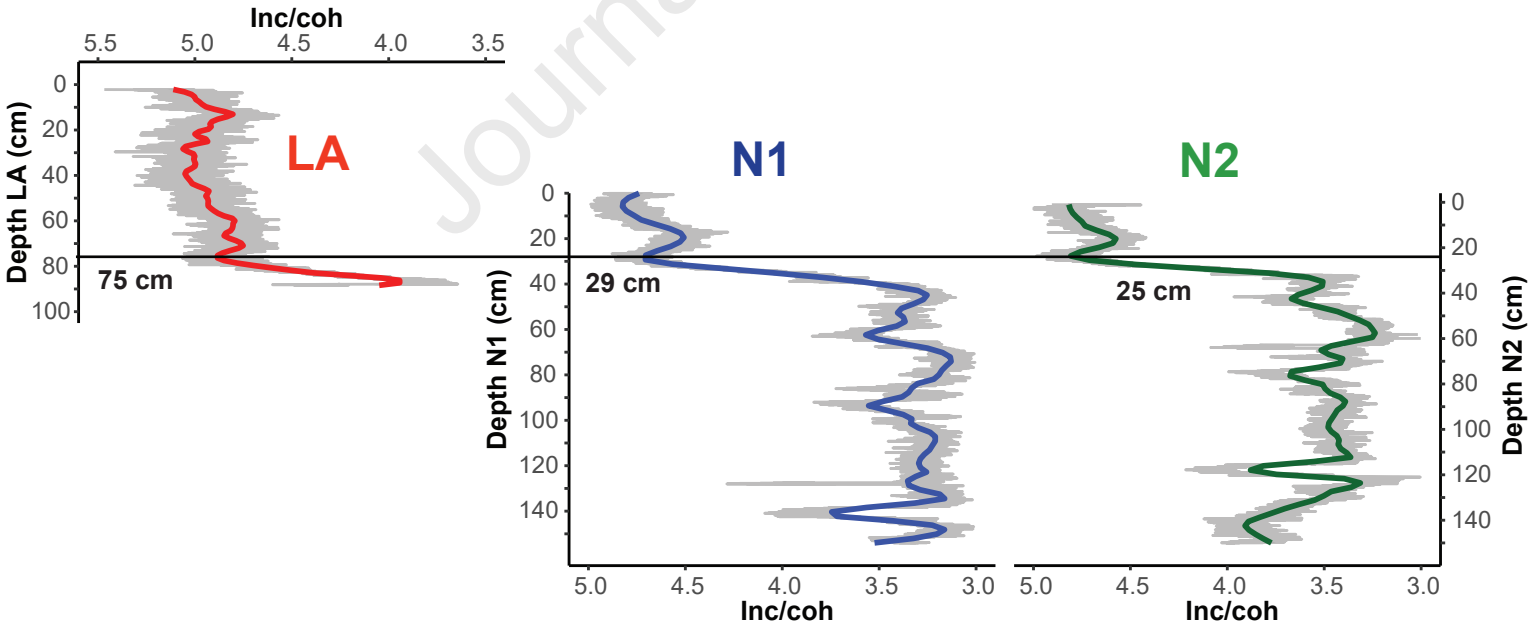

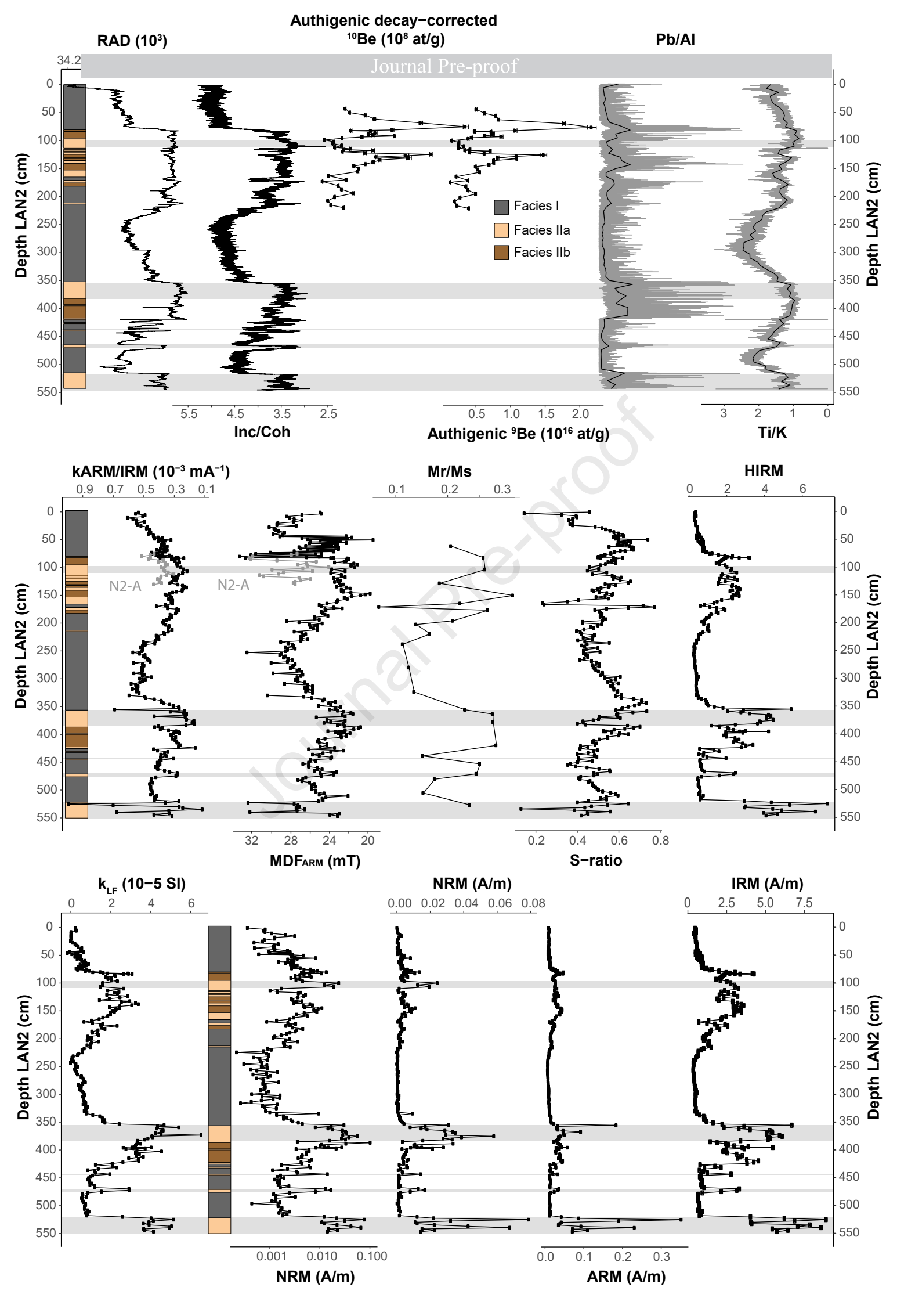
Authigenic decay−corrected
RAD (10³)
¹⁰Be (10⁸ at/g)
Pb/Al
Journal Pre-proof
Facies I
Facies IIa
Facies IIb
Depth LAN2 (cm)
Inc/Coh
Authigenic ⁹Be (10¹⁶ at/g)
Ti/K
kARM/IRM (10⁻³ mA⁻¹)
Mr/Ms
HIRM
N2-A
N2-A
MDFARM (mT)
S−ratio
kLF (10−5 SI)
NRM (A/m)
IRM (A/m)
NRM (A/m)
ARM (A/m)

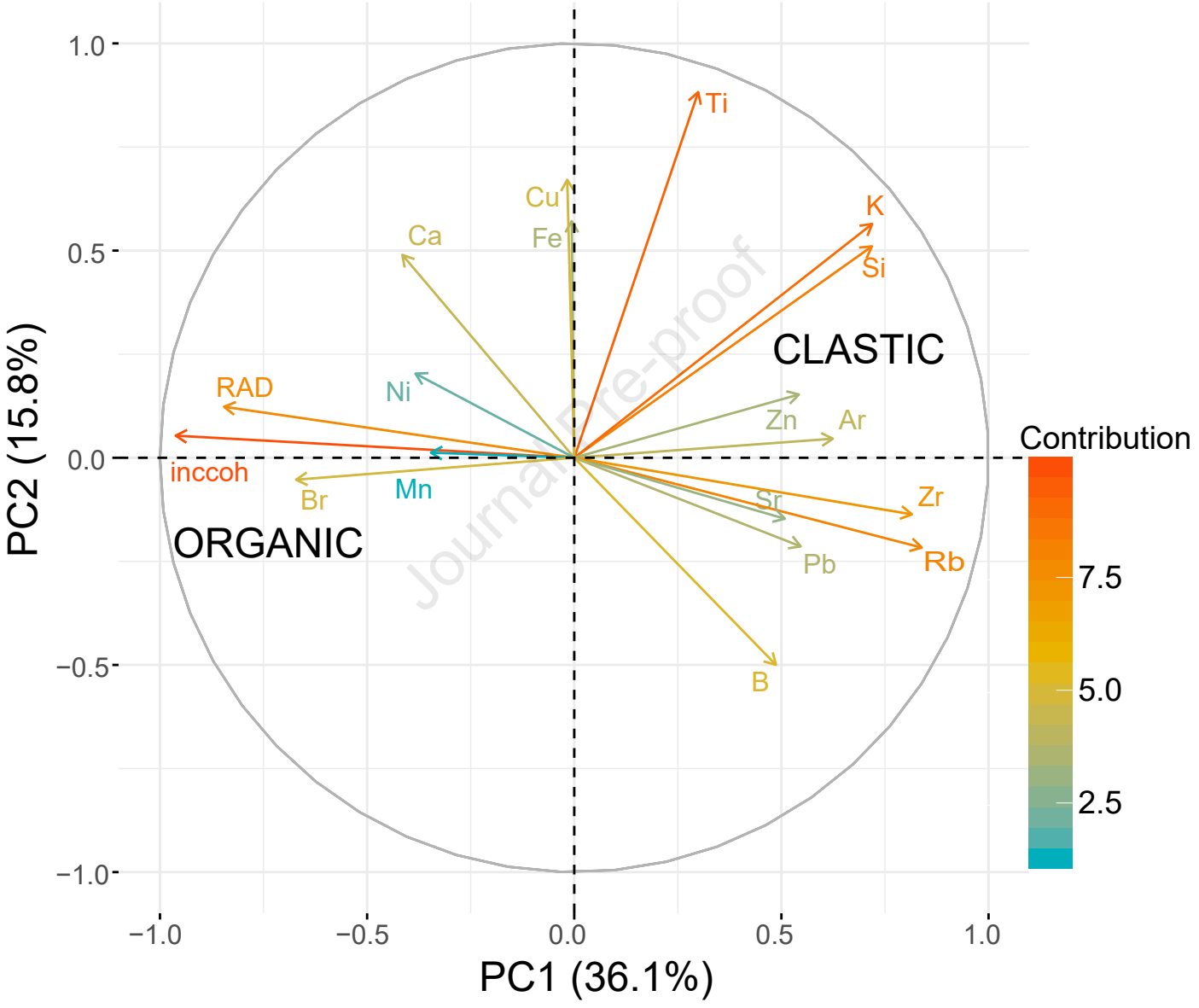

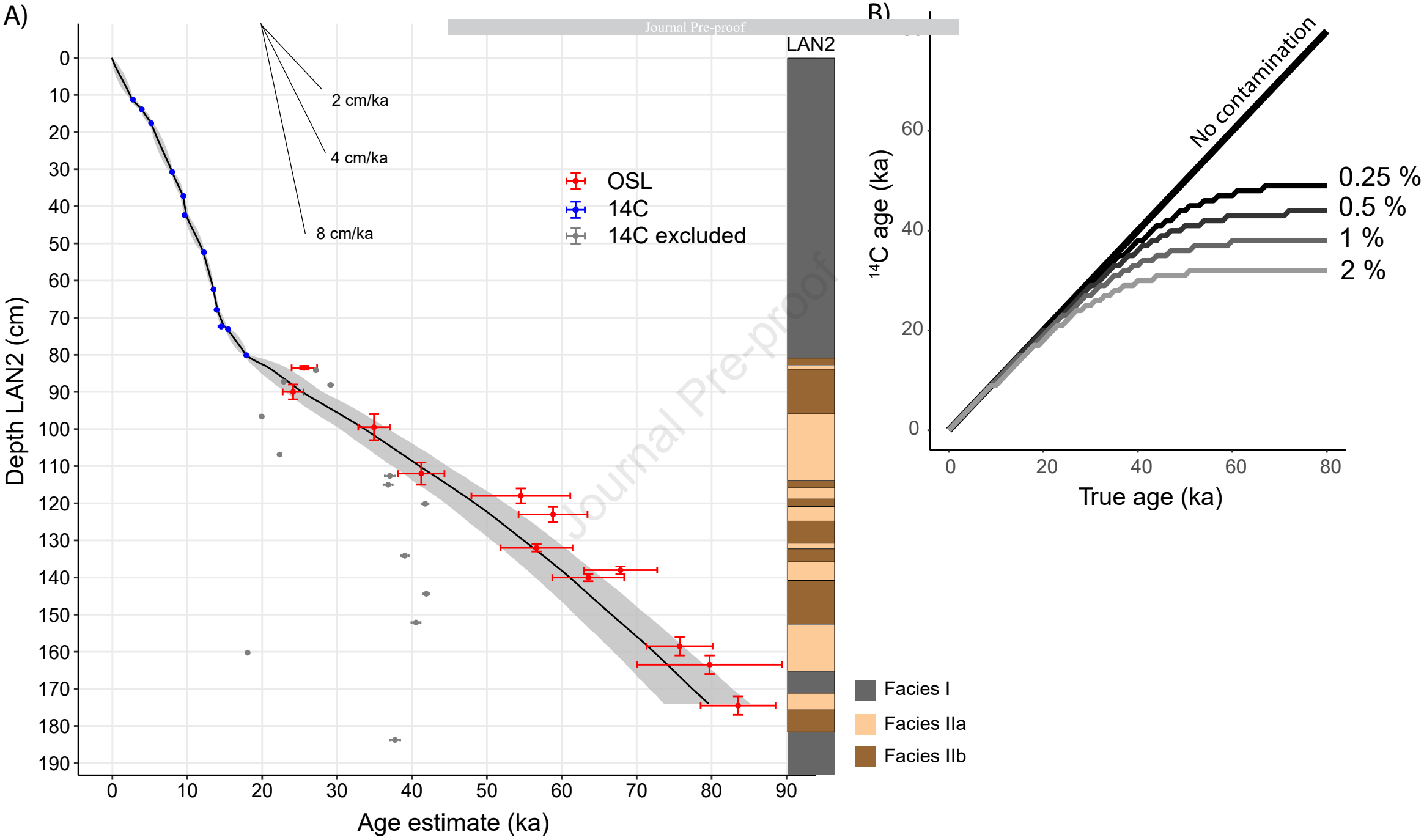

Facies I -Interglacial sediments

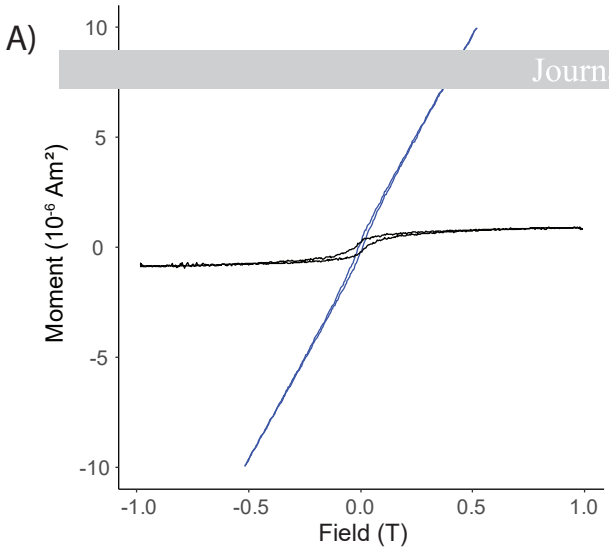

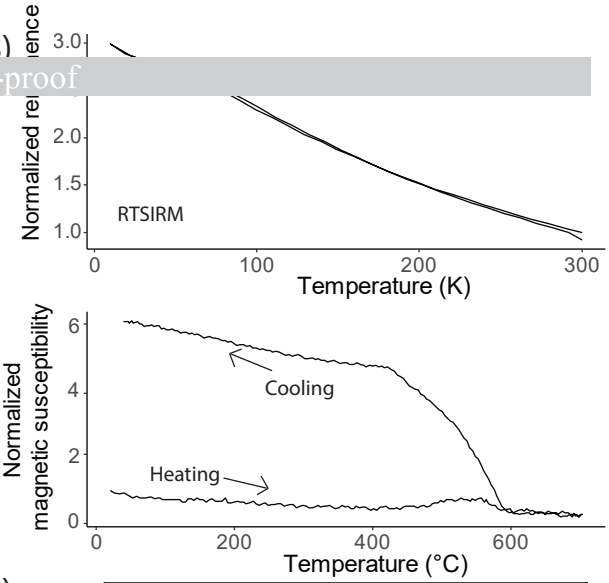

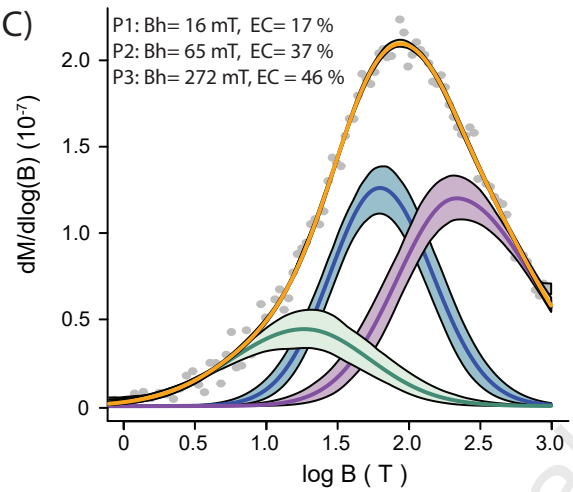

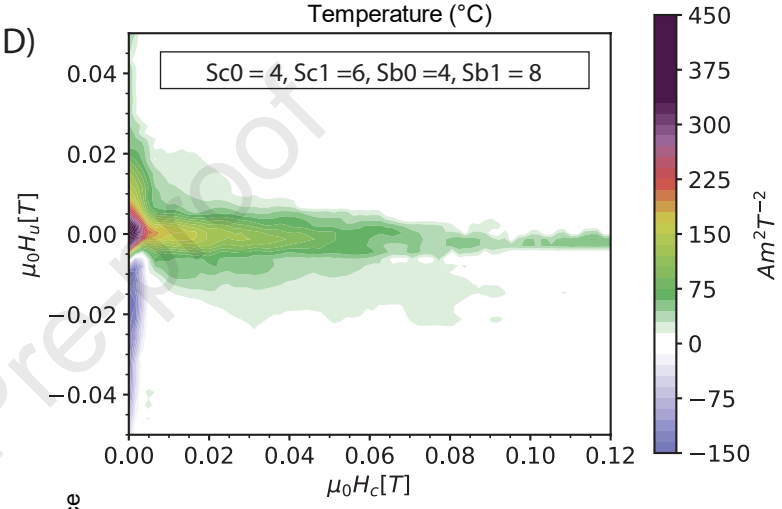

Facies II -Glacial sediments

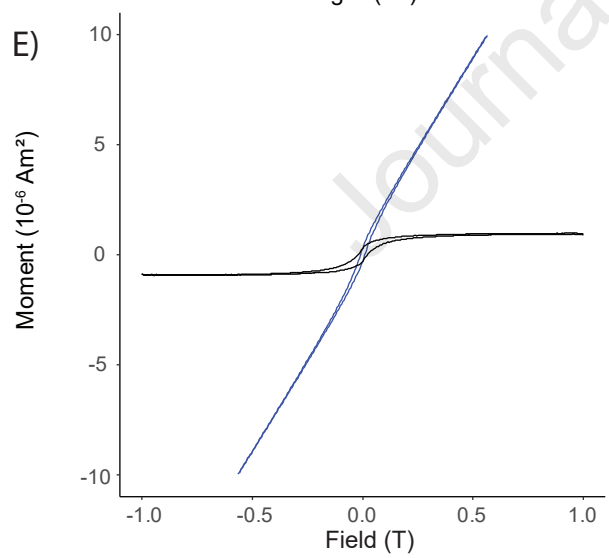

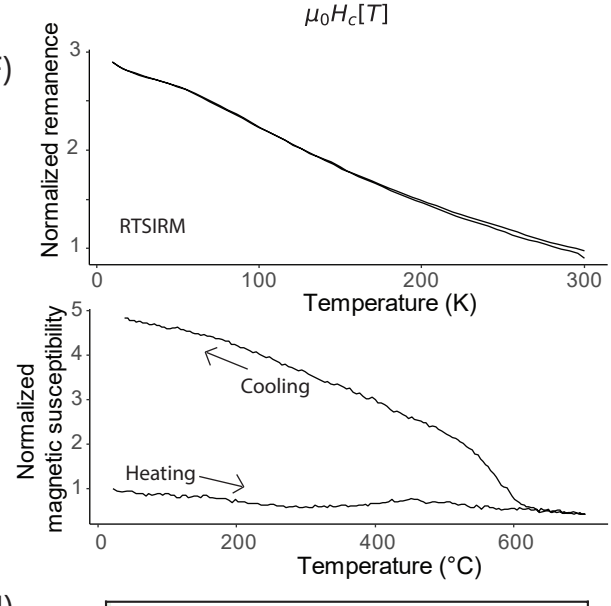

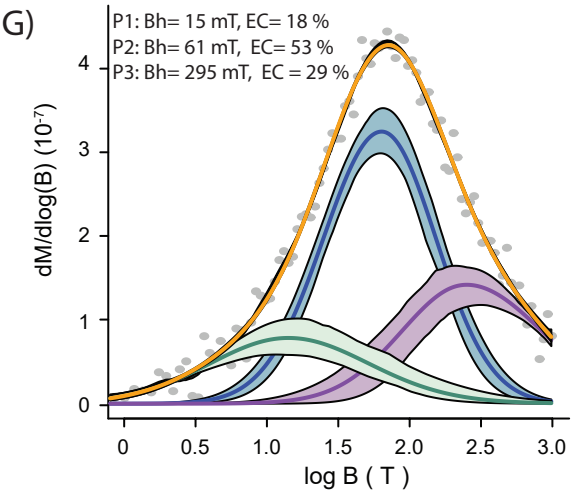

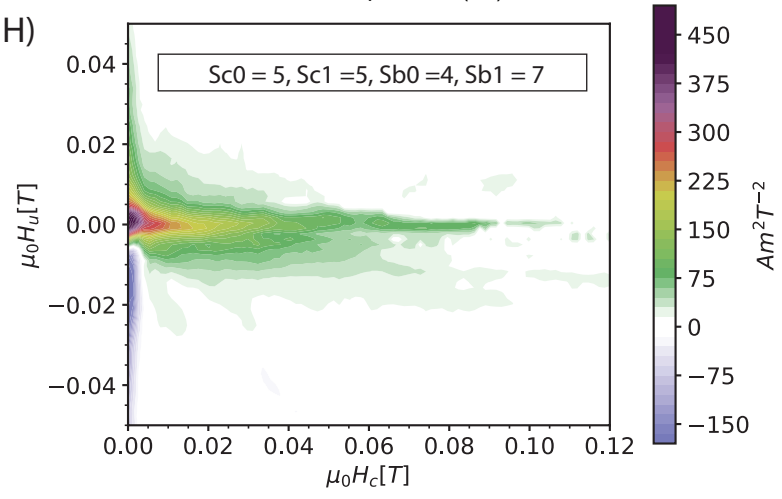

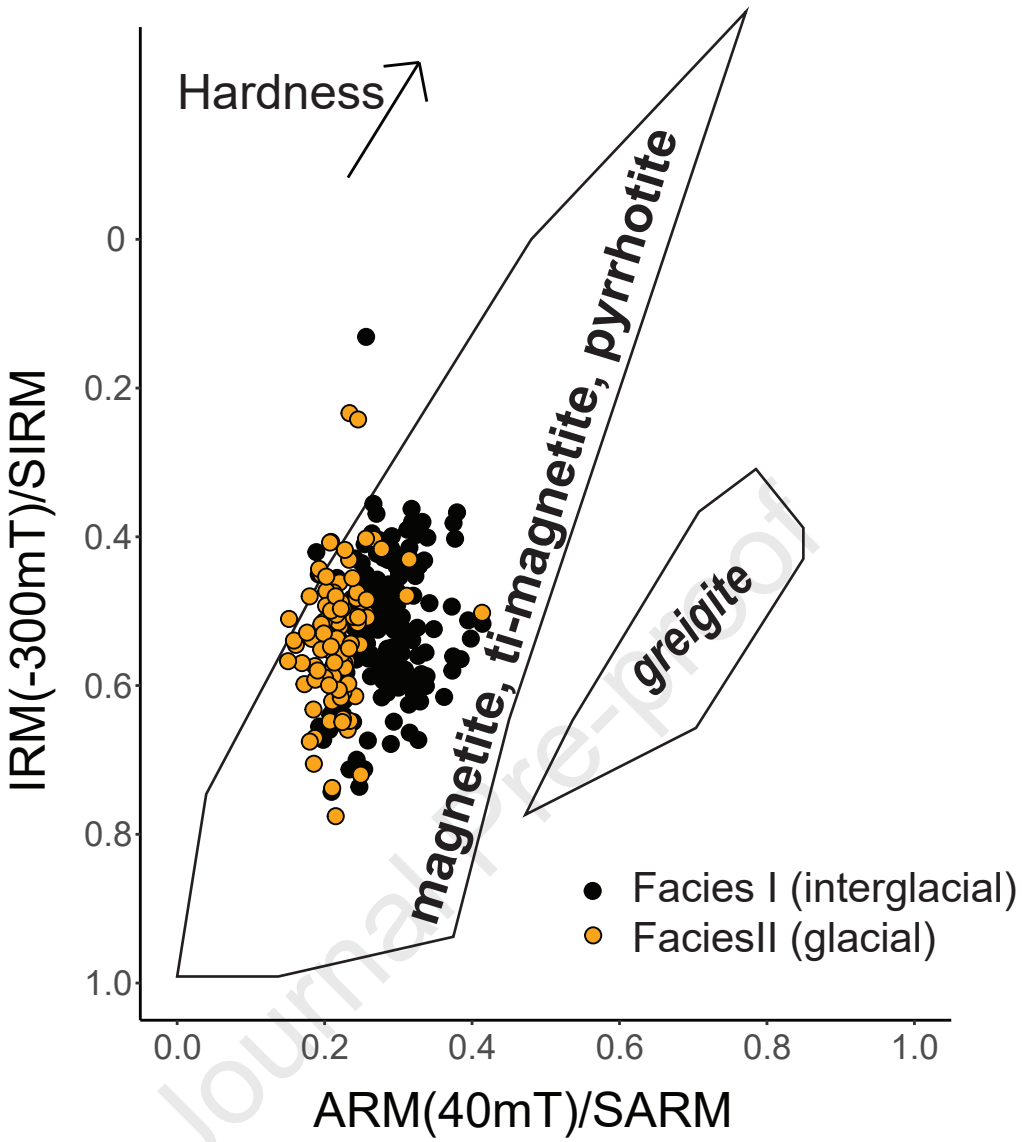

PALEOMAGNETIC DIRECTIONS

A) RAW D … IAD<20)

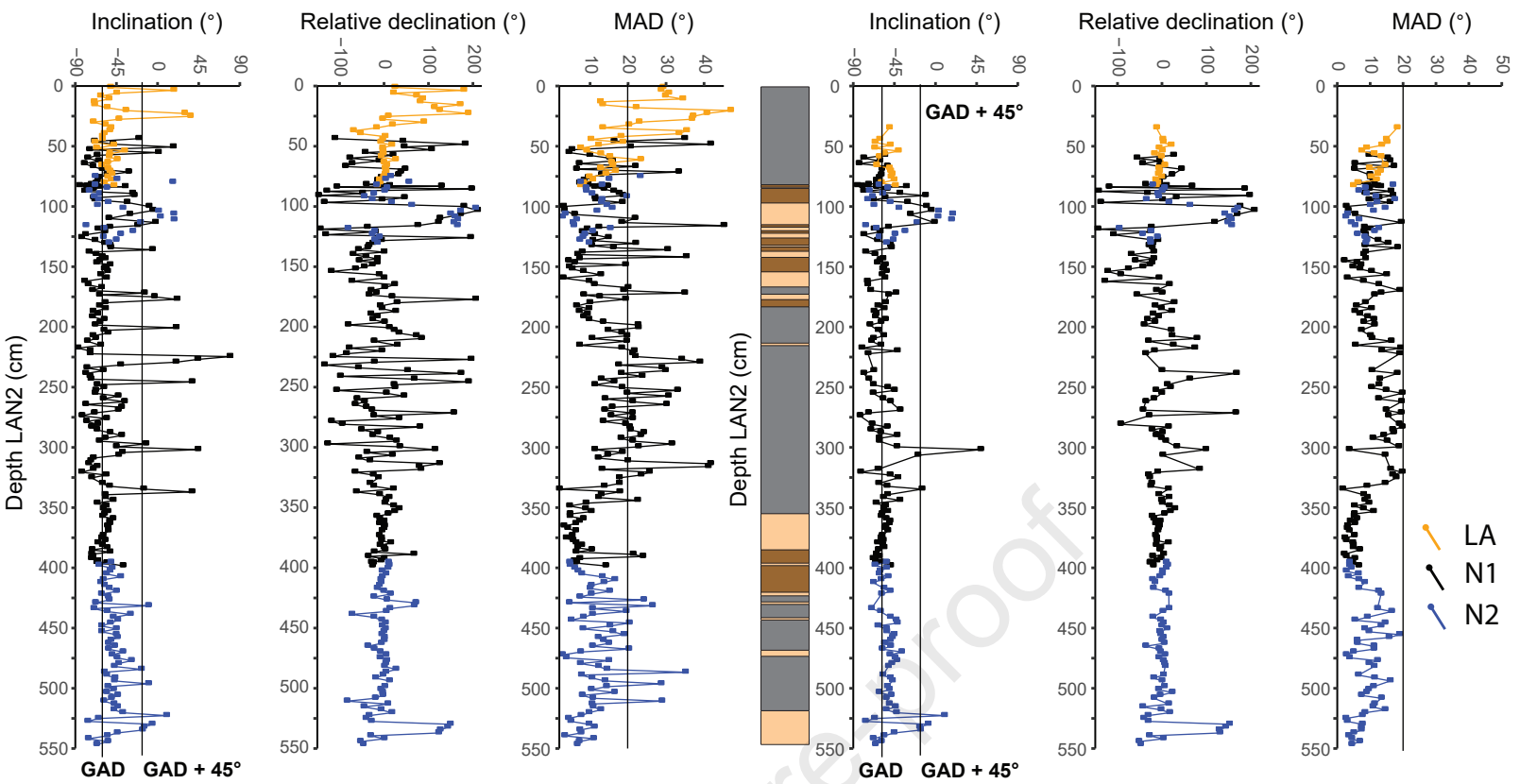

RELATIVE PALEOINTENSITY ESTIMATES

C) RAW DATA

D) SELECTED

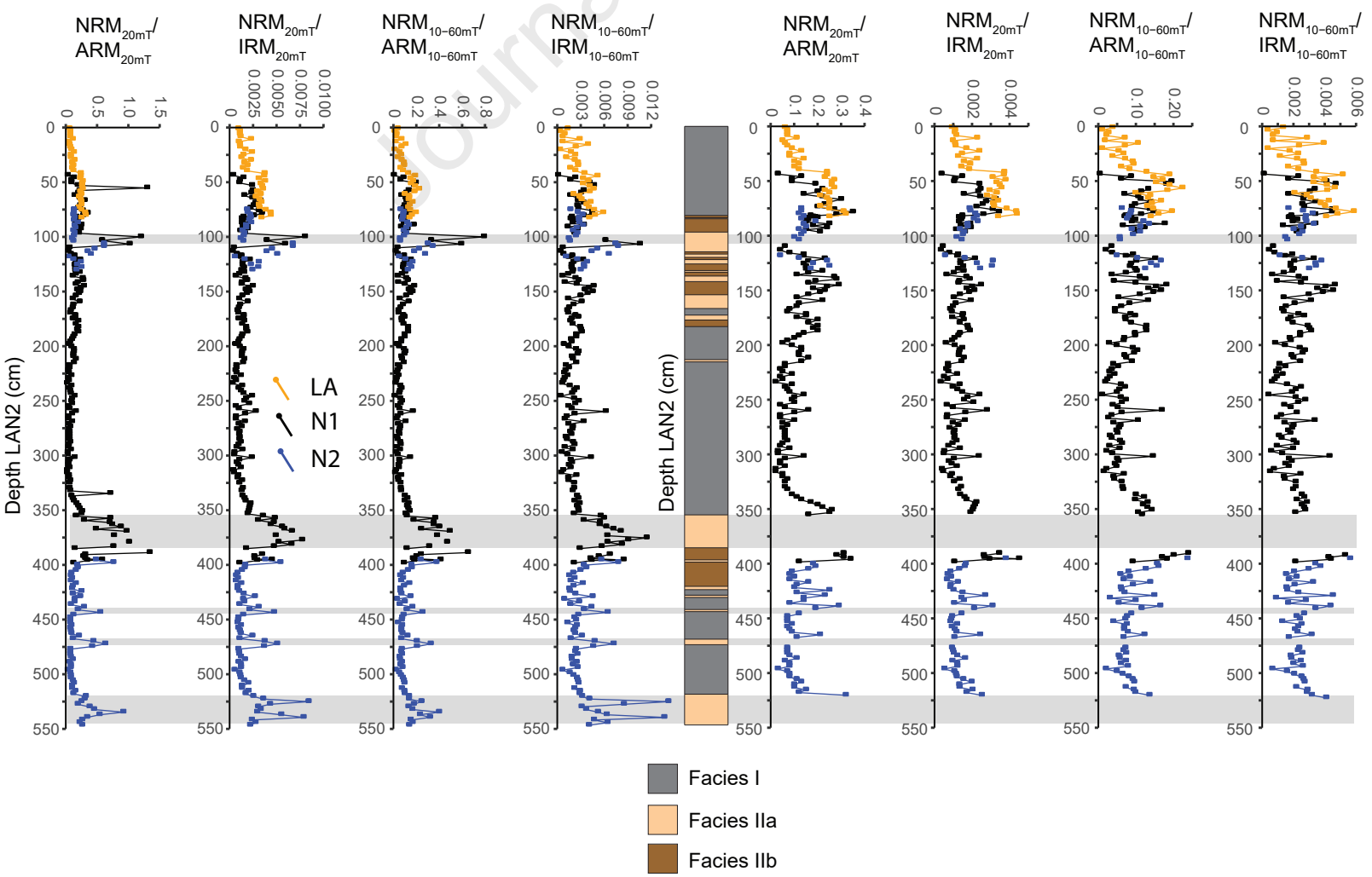

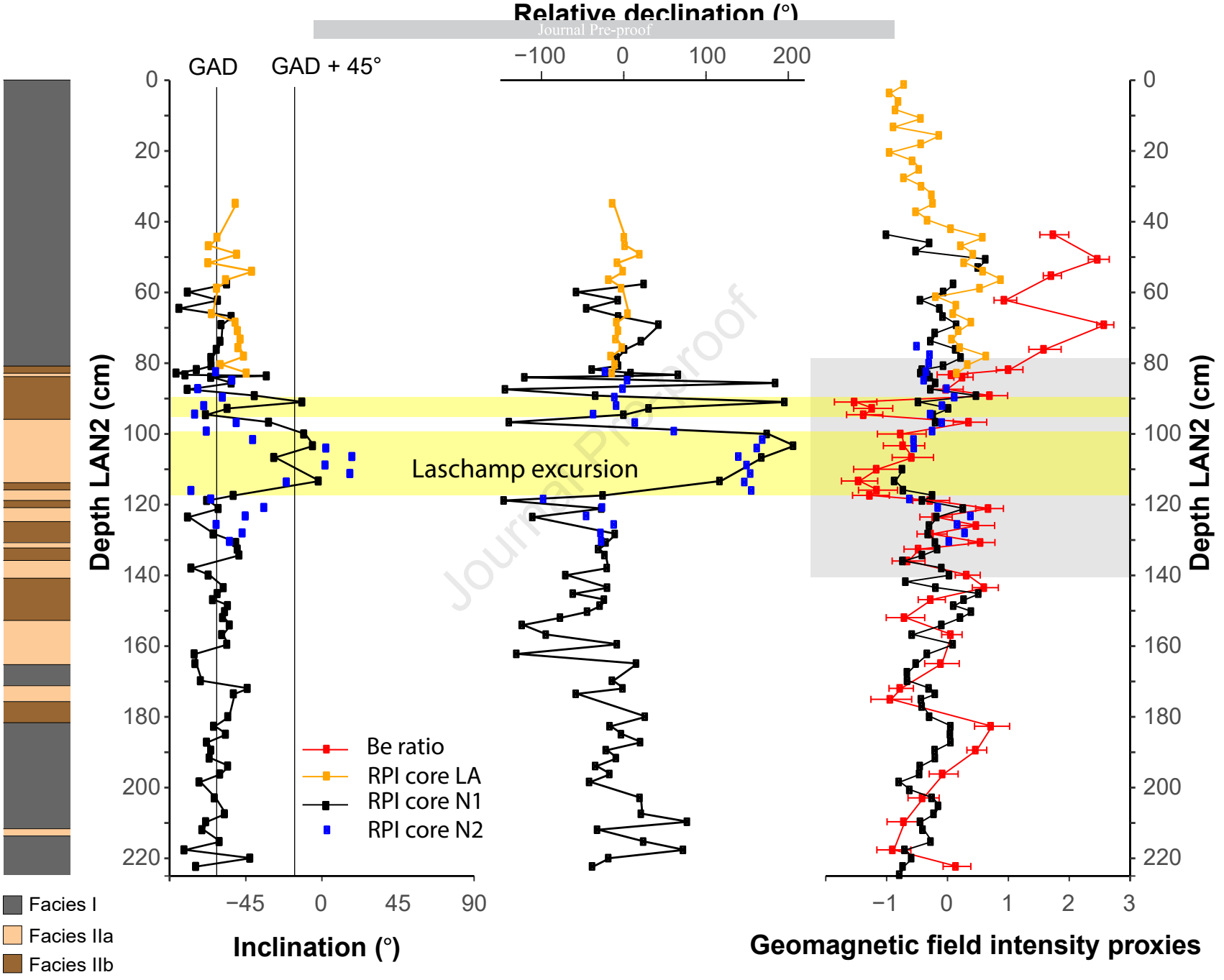

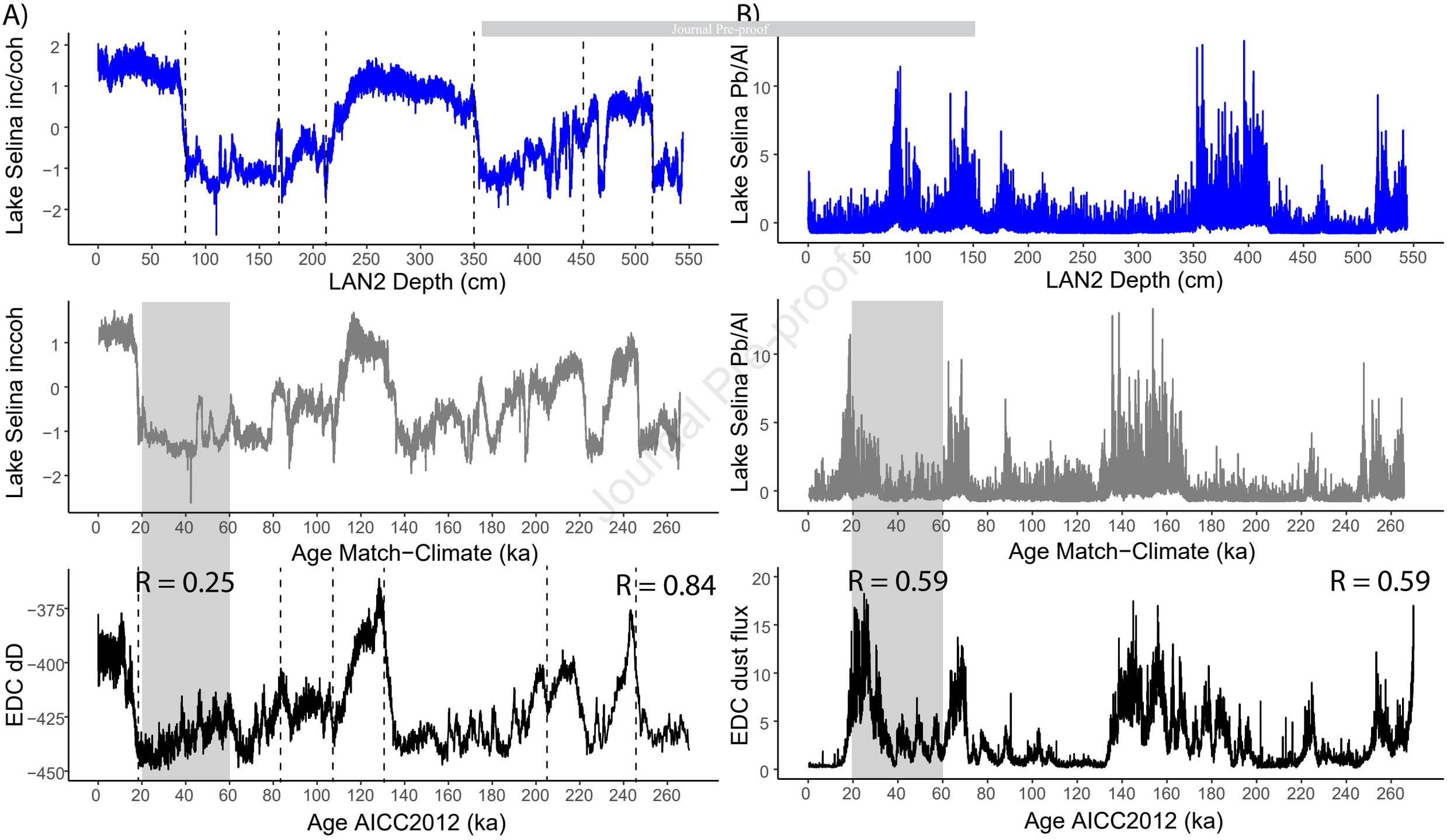

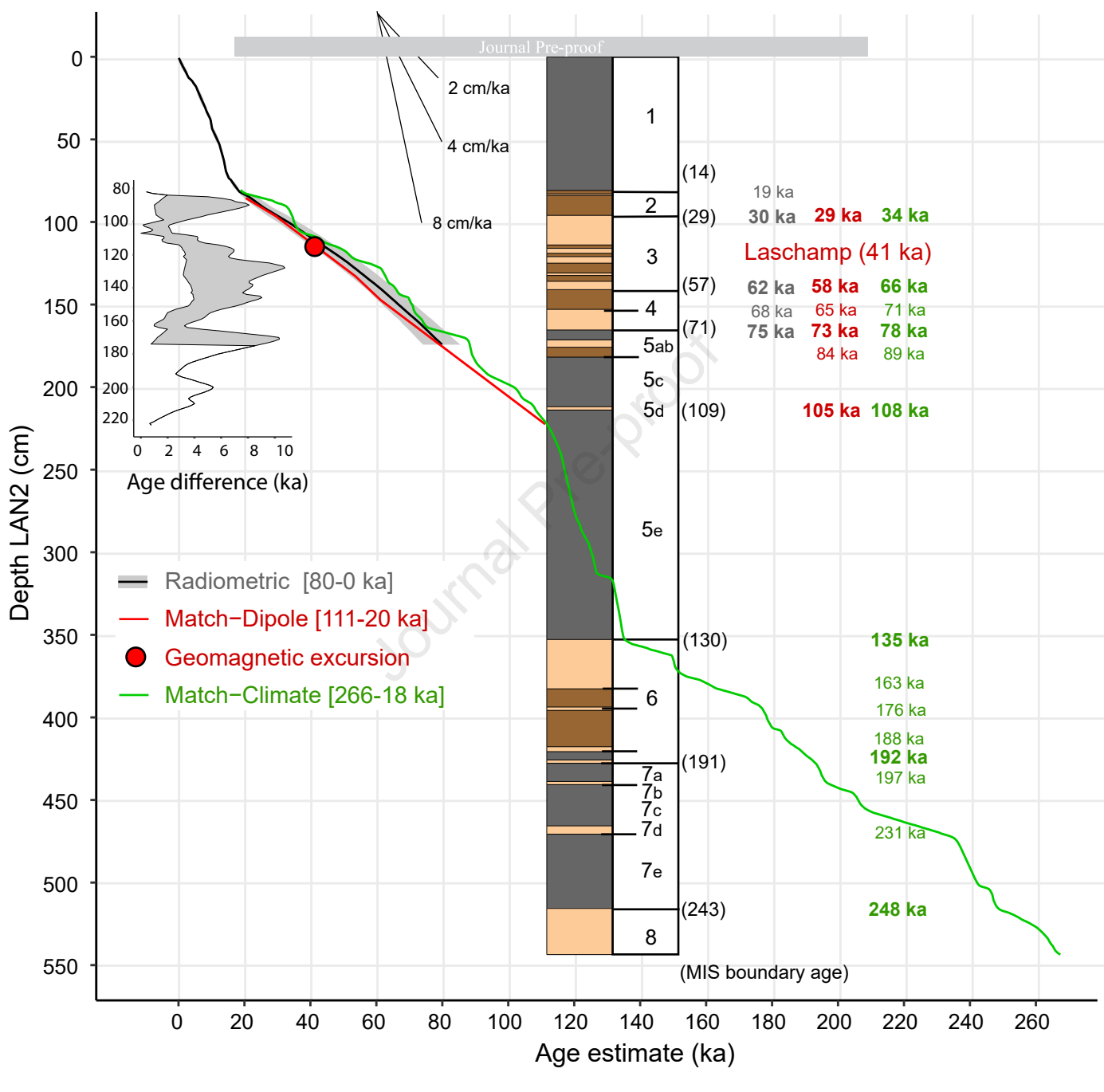
Journal Pre-proof
2 cm/ka
4 cm/ka
8 cm/ka
Age difference (ka)
Radiometric [80-0 ka]
Match−Dipole [111-20 ka]
Geomagnetic excursion
Match−Climate [266-18 ka]
1
2
3
4
5ab
5c
5d
5e
6
7a
7b
7c
7d
7e
8
(14)
(29)
(57)
(71)
(109)
(130)
(191)
(243)
(MIS boundary age)
19 ka
30 ka
29 ka
34 ka
Laschamp (41 ka)
62 ka
58 ka
66 ka
68 ka
65 ka
71 ka
75 ka
73 ka
78 ka
84 ka
89 ka
105 ka
108 ka
135 ka
163 ka
176 ka
188 ka
192 ka
197 ka
231 ka
248 ka
Depth LAN2 (cm)
Age estimate (ka)

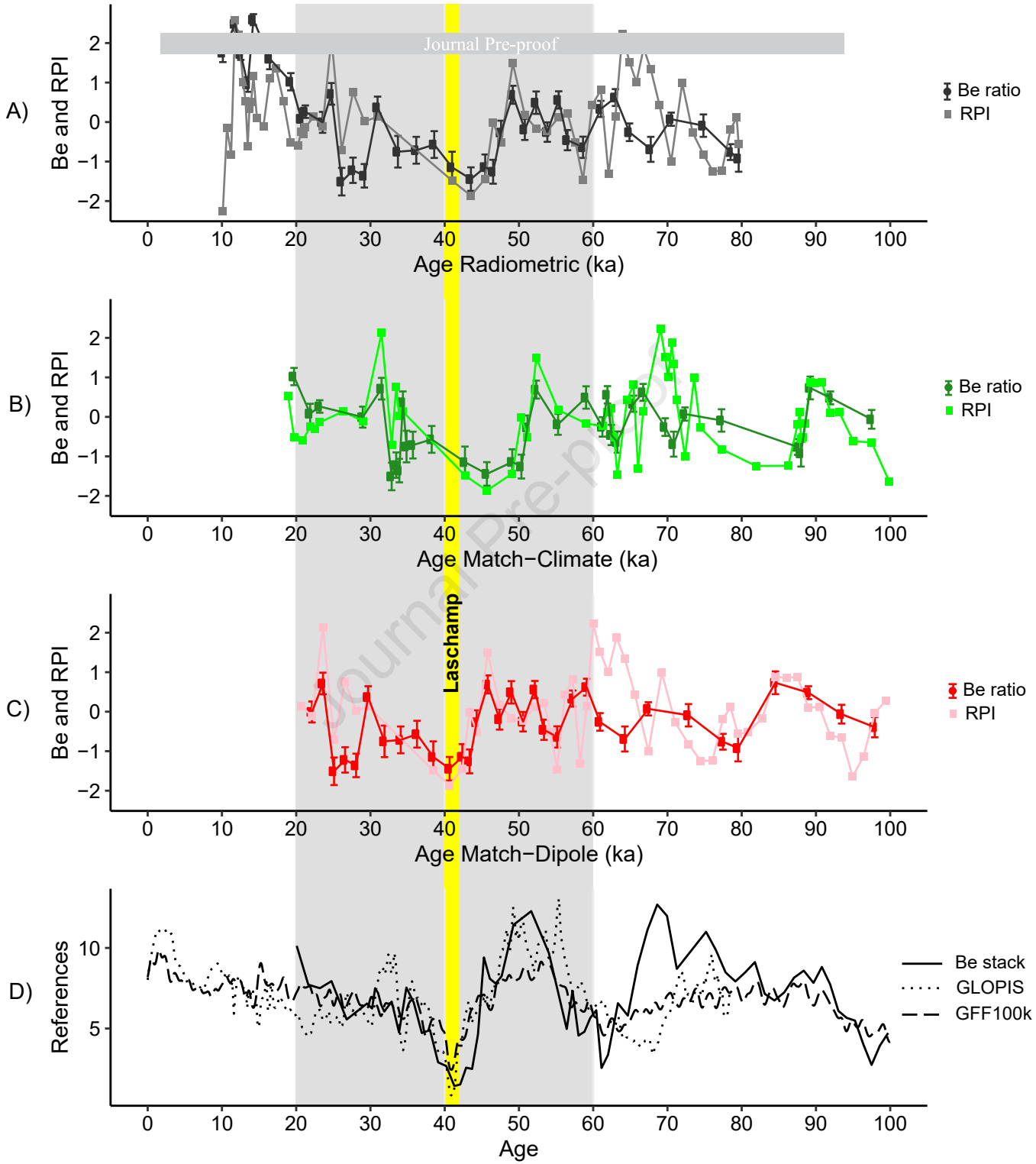
A)
B)
C)
D)
Be and RPI
References
Age Radiometric (ka)
Age Match−Climate (ka)
Age Match−Dipole (ka)
Age
Laschamp
Be ratio
RPI
Be stack
GLOPIS
GFF100k
Journal Pre-proof

Declaration of interests

☒ The authors declare that they have no known competing financial interests or personal relationships that could have appeared to influence the work reported in this paper.

☐The authors declare the following financial interests/personal relationships which may be considered as potential competing interests: